Experimental investigation of the flow past passive vortex generators on an airfoil experiencing three-dimensional separation

Marinos Manolesos[1], Spyros G. Voutsinas

Laboratory of Aerodynamics, National Technical University of Athens, 9 Heroon Polytechneiou str., 15780 Athens, Greece.

Abstract

The use of passive vortex generators (VGs) as a simple and effective way to delay or suppress separation on an airfoil optimized for wind turbine blades is examined experimentally. The profile experiences three-dimensional separation of the Stall Cell type. Pressure, Flow Visualization and Stereo Particle Image Velocimetry experiments are discussed for the case of triangular counter rotating VGs with common flow up. For a Reynolds number of 0.87×10^6, Stall Cell formation is delayed for 5°, and lift increases up to α = 15°. In total, maximum lift increases by 44%, while drag increases by 0.002 at pre-stall angles of attack. At α = 16° the flow bifurcates between separated and attached flow conditions. At α = 10° the flow is examined in detail and an investigation on the turbulence characteristics is carried out by correlating Reynolds stresses production to time averaged flow gradients. Strong turbulent interaction is observed between the two vortices and the underlying flow up to 37.2 VG heights downstream of the VGs, while further downstream (up to 47.2 VG heights) diffusion governs the flow. A wandering motion of the VG vortices leads to increased $\overline{v'v'}$ normal stress values between the two vortices.

Keywords

Passive Vortex Generators, Stall Cells, Stereo Particle Image Velocimetry

Nomenclature

$A_{0.1}$	area surrounded by the ω = 0.1ω$_{max}$ isoline
Cd	Drag coefficient
Cl	Lift coefficient
D	Distance between two VG pairs
L_m	Interrogation area length
$P_{u_iu_j}$	Reynolds stress production tensor
$R_{0.1}$	Vortex radius up to ω = 0.1ω$_{max}$
U	Normalized time averaged streamwise velocity
U_{inf}	Free stream velocity
U_{res}	Minimum resolvable velocity
V	Normalized time averaged vertical velocity
$V_i(y,z)$	Vortex velocity field
$U_i(y)$	mean flow velocity field
W	Normalized time averaged spanwise velocity

[1] Corresponding author, E-mail: marinos@fluid.mech.ntua.gr, Tel: +30 210 772 4385, Fax: +30 210 772 1057

c	Chord
d	spanwise distance between the LE of two VGs of the same pair
h	Vortex generator height
l	Vortex generator length
r_c	Vortex radius
$u_i(y,z,t)$	Instantaneous velocity field
$u_{i,PIV}(y,z)$	time averaged velocity filed
$\overline{u_i'u_j'}$	Reynolds stress tensor
x	Chordwise coordinate
x_{VG}	Chordwise position of the vortex generator trailing edge
y	Vertical coordinate
z	Spanwise coordinate
α	Angle of attack
Δx	Distance from the vortex generator trailing edge
ΔCd	Increase in drag due to the use of vortex generators
β	VG angle to the free stream flow
δ	Boundary layer height
ω	Vorticity
ω_{max}	Peak vorticity
BL	Boundary Layer
HL	High Lift
LE	Leading Edge
LHS	Left Hand Side
LL	Low Lift
NTUA	National Technical University of Athens
PIV	Particle Image Velocimetry
RANS	Reynolds Averaged Navier-Stokes
Re	Reynolds
SC	Stall Cell
TE	Trailing Edge
TKE	Turbulent Kinetic Energy
VG	Vortex Generator
ZZ	Zigzag
3D	Three-dimensional

1 Introduction

Flow separation on aerodynamically shaped bodies is an unfavourable state often appearing over part of the operational envelope. Due to its implications on performance and reliability, numerous technologies have been developed in order to control or suppress separation [1, 2]. Among them, passive vortex generators (VGs) are one of the simplest and most effective techniques available. Examples of successful use of passive VGs include, but are not limited to airfoils [3, 4], highly swept wings [5], bluff bodies [6], wind turbines [7], noise reduction [8] and internal flows [9]. In the present work the ability of VGs to suppress three-dimensional (3D) separation over a wing model is examined.

It has been long known [10] that, at high enough angles of attack, the separated flow on a wing can be highly 3D, as coherent vortical structures known as Stall Cells (SCs) may form. SCs consist of a pair of counter rotating vortices [11, 12] and are formed on airfoils that experience Trailing Edge (TE) type of stall or a combination of Leading Edge (LE) and TE type of stall [13]. Recently, the onset of SCs has been reported on wind tunnel models of airfoils designed for or used on wind turbine blades [11, 12, 14-16], as well as on wind turbine blades at standstill [17, 18]. Despite the fact that SCs have been widely encountered there is limited research on their control using VGs or in fact any other device.

In this context, the present study aims at (a) examining whether VGs can control SC formation and (b) analysing in detail the flow downstream of the VGs based on Stereo PIV recordings. This is the first time that the suppression of SC formation using VGs is investigated thoroughly. Furthermore, while detailed studies of VG induced flow on flat plates have been published in the past (e.g. [19-21]) there is limited research for the case of an airfoil flow (e.g. [15]) at high Re number.

The paper begins with a short overview of previous work on the flow past VGs and on SCs, as a pertinent manifestation of 3D separation on airfoils/wings. Then the experimental set up is described and, next, the experimental data are presented and discussed in terms of the mean flow and turbulence characteristics. The paper ends with a summary of the main findings. An extended description of the experimental configuration is given in the Appendix. All experimental data are freely available in the public domain[2]. A comparison with numerical results can be found in [22].

1.1 Previous Work

1.1.1 Passive Vortex Generators

The working principle and the underlying mechanisms of VG flow have been adequately described by various researchers, e.g. [23-25]. In brief, VGs favourably affect a separated boundary layer (BL) by bringing high momentum flow from the free stream closer to the solid surface and thus re-energizing the near wall flow. This is done by the tip vortices, shed from the free tips of the VGs.

Since the first application of VGs on a wing [26], the literature on VGs as passive flow control devices has been quite extensive. Several studies [27-32] have provided design guidelines

[2] http://www.aerolab.mech.ntua.gr/3D%20separation%20control.rar

under various flow conditions. The main focus has been on zero- and adverse-pressure gradient flows on a flat plates and bumps, while detailed studies of the flow past VGs on airfoils remain limited.

Pearcey [29] applied inviscid theory to predict the vortex paths downstream of counter and co-rotating VGs. It was suggested that counter rotating vortices will eventually move away from the surface under mutual interaction; a mechanism that has been observed in various studies [24, 33, 34]. For the co-rotating vortices a lateral displacement under the influence of their image vortices was predicted, with no upward movement. In [35] it was found that counter rotating vortices with common downwash grow within the developing Boundary Layer (BL) under adverse pressure gradient and as a result they do move away from the solid surface. This is a viscous effect that the inviscid analysis in [29] could not predict.

In general, VG vortices become less concentrated and weaker in strength, while peak vorticity drops at a higher rate than circulation due to diffusion [24]. The drop in circulation is linked to viscous dissipation and hence it is greater for vortices generated by low-profile VGs ($h < \delta$) [36]. In the same study it was also found that for a single VG in a zero pressure gradient flow circulation dropped faster for vortices with greater initial strength (VGs at higher angle).

For a single vortex in a zero pressure gradient BL the distribution of the turbulence quantities can be considered as the distortion of a boundary layer turbulence by a superimposed vortex [34]. Flow complexity increases when a pair of counter rotating vortices are present, in which case a significant increase in the vertical and lateral velocity deviations is observed [33]. In [35] these peaks were linked to vortex wandering, while high $\overline{v'v'}$ values were also measured at the centre of a laterally meandering vortex [37]. Despite the significant changes caused by the presence of the VG vortices, the state of anisotropy remains unchanged in the near wall region, since it is determined by the presence of the solid surface.

1.1.2 Stall Cells

SCs appear on the suction side of wings at angles of attack around maximum lift. They have been reported on wing models with various types of tip treatment (wall to wall models with or without wall suction [10, 38], tip with endplates [39], free tip [40]), and can form on both low and high aspect ratio (AR) wings (from AR = 1.5 in [41] to AR = 12 in [42]). It is widely agreed that for sufficiently high Re number ($Re > 0.3 \times 10^6$) and turbulence intensity (T.I. > 0.1%) SCs are dynamic structures. They have been reported to move in the spanwise direction [39, 43] or even form and disappear in a seemingly random manner [10, 44].

In [45] it was found that the inherently unstable SCs can be stabilized by means of a large enough spanwise disturbance. In more detail, a zigzag (ZZ) tape was applied on the wing suction surface (at its centre for 10% of its span), which acted as a stabilizing mechanism. The ZZ tape effectively forced the flow to form a single stable SC. It is noted that the ZZ tape was not the generating mechanism for the SCs, which would form on the wing suction surface with or without the localized disturbance. The flow with the ZZ tape had the same amount of separated flow for angles of attack $\alpha > 9°$ and for Re numbers ranging from 0.5×10^6 to 1.5×10^6. It was concluded that the ZZ tape effectively forces the flow to select one

of the possible modes. In the present study the same stabilization mechanism and the same wing model examined in [11, 12, 45] were used.

With regard to SC control, the first and only documented successful attempt to delay SC formation using VGs was done by Moss and Murdin [46] on a NACA 0012 airfoil, at Re numbers of 0.9×10^6 and 1.7×10^6. More than four decades later, Velte and Hansen [41] reported the onset of SCs at post-stall angles of attack on a DU 91-W2-250 profile with VGs, also at a Re number of 0.9×10^6. Table 1 below lists the published studies where VGs were applied on airfoils exhibiting SC formation.

Study	Moss & Murdin, 1971, [46]	Storms & Jang 1994, [47]	Velte & Hansen 2012, [41]	Present study
Airfoil	NACA 0012	NACA 4412	DU 91-W2-250	NTUA-t18
Re [x10^6]	0.86, 1.68	2.0	0.9	0.87
VG type	Vanes	Wishbones	Vanes	Vanes
VG height	0.016c	~3.5δ	0.5δ	δ
VG position	10% airfoil chord	12% airfoil chord	0.3% airfoil chord	0.3% airfoil chord
Method	Pressure measurements	Pressure measurements	Stereo PIV	Pressure measurements, Stereo PIV
Stall Cells?	First mention of VGs applied on a wing that exhibits SC formation	3D separation is mentioned but not examined further.	SCs are simply mentioned for the case with VGs, at post stall	VGs are specifically used to prevent SC formation

Table 1: Investigations regarding 3D separation control using VGs.

2 Experimental approach

The tests concerned an 18% thick airfoil optimized for use on variable pitch and variable speed multi MW blades [48]. All experiments were carried out in the 1.4×1.8m (height × width) test section of the National Technical University of Athens (NTUA) wind tunnel. A schematic view of the test set up is given in Figure 1. The wing spanned the test section vertically and fences were used in order to minimize the effect of the wind tunnel wall boundary layer. A detailed description of the experimental set up is given in the Appendix, while the main points are outlined in this section.

The central VG pair was studied in this investigation, i.e. the one that was located downstream of the ZZ tape and was always met by turbulent flow. The pressure taps were also located at the centre of the wing span, downstream of the stabilizing disturbance.

All Stereo PIV measurements were taken at α = 10°. The flow was measured on three planes normal to the free stream, downstream of the central VG pair, at x/c = 0.6 (plane A), x/c = 0.7 (plane B) and x/c = 0.8 (plane C), see Figure 2. With respect to their distance from the VG TE (Δx), planes A, B and C were at Δx = 27.2h, 37.2h and 47.2h, respectively. Δx is defined as

$$\Delta x \equiv x - x_{VG} = x - 0.328c \quad (1)$$

where x_{VG} is the VG TE location and c is the wing chord.

For each plane 2000 snapshots were taken and the results presented here are the averaged data. All data in the present paper refer to a wing of AR 2.0 at a Re number of 0.87×10^6. Data are non-dimensionalized with the wing chord and the free stream velocity ($U_{\inf}$), unless otherwise stated. Further details on the measurement planes are given in Table 2.

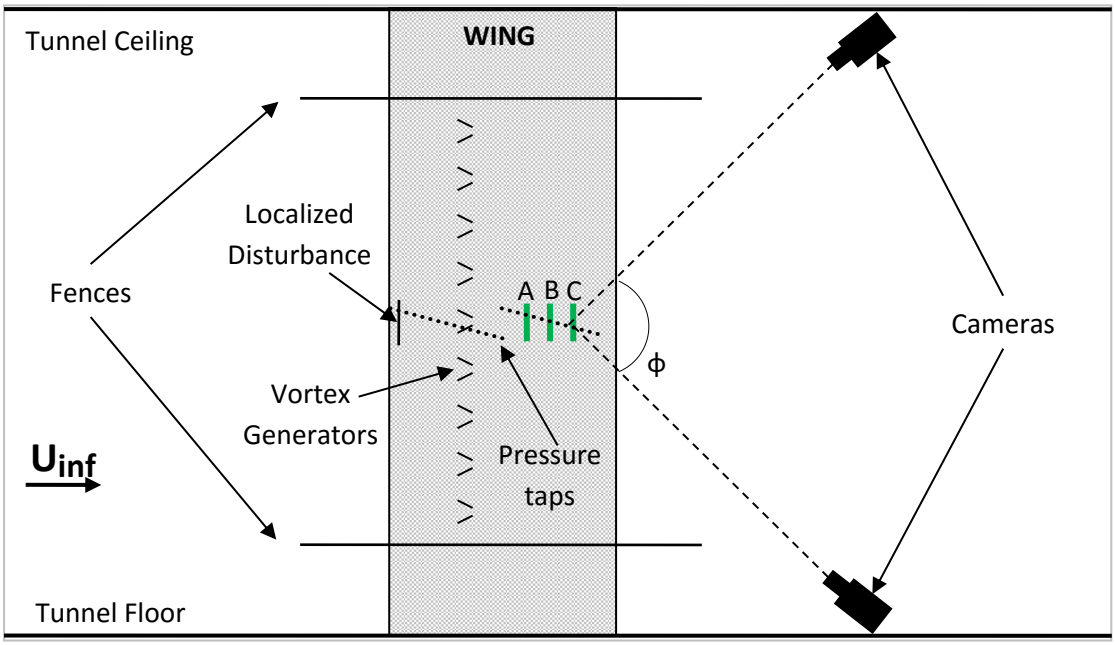

Figure 1: Schematic planform view of the test set up showing the wing, the fences, the pressure taps at the centre of the wing span, the stabilizing disturbance and the Stereo PIV cameras along with the measurement planes at x/c = 0.6 (plane A), x/c = 0.7 (plane B) and x/c = 0.8 (plane C). The camera contained angle (ϕ) for plane C is also indicated.

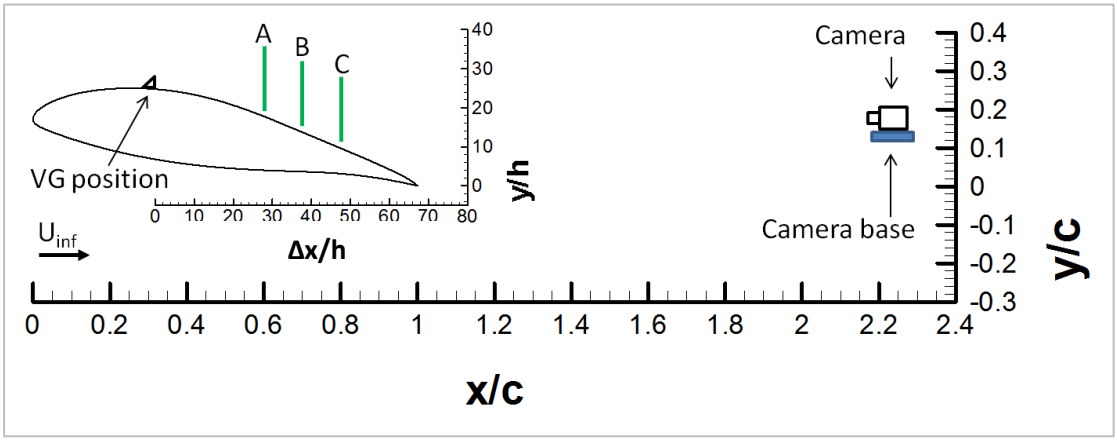

Figure 2: Schematic top view of the test set up. Measurement planes A, B and C are shown with solid green lines. Two sets of axes are shown: the (x/c, y/c) set is scaled with the wing chord (c) with its x-axis starting at the wing LE, while the (Δx/h, y/h) set is scaled with the VG height (h) with its x-axis starting at the VG TE (see Eqn. (1)). In both sets y = 0 corresponds to the wing TE. Cameras were located 1.2c downstream of the wing TE.

	Plane A	Plane B	Plane C
Chordwise location	0.6c	0.7c	0.8c
Distance from VG trailing edge [h]	27.2	37.2	47.2
Lenses	150mm	150mm	150mm
Camera contained angle (ϕ)	62°	65°	69°
Final interrogation area size [px]		16	
Final interrogation area size [mm]		0.8	
Minimum resolvable velocity [m/s]		0.4	
Minimum resolvable velocity [normalized with respect to the free stream]		2%	
Number of Snapshots		2000	

Table 2: Stereo PIV test details for all the planes measured

Camera positioning effect and vibration analysis

The cameras were located inside the test section, 1.2c downstream of the wing TE (see Figure 2). The camera base was secured on elastic anti-vibrating pads and both cameras were mounted on reinforced Scheimpflug angle adjustable mountings. Placing the cameras inside the test section raised two issues: a) whether and how the cameras affected the flow over the wing model and b) whether the cameras vibrated and, if yes, what the effect of this vibration on the results was.

Regarding the first issue, pressure measurements on the wing surface taken with and without the cameras were practically identical so it was concluded that the cameras and the camera base did not affect the flow on the wing.

In the past several researchers encountered the issue of camera vibration. Some applied a frame by frame correction to the measurements [49, 50], whereas others attributed non-physical variation of the measured rms data to camera vibration [51, 52].

In the present case camera vibration was examined using a procedure similar to that described in [49, 50], using the wing TE position as a reference. However, during the actual measurements the wing TE edge was out of focus so it was not possible to apply a frame by frame correction. Instead the error introduced by the camera vibration was quantified and, as explained below, it was found to be negligible.

The position of the TE was obtained with sub-pixel accuracy using a 3rd order curve fit on the light intensity data over a series of photos, as suggested in [49]. By analysing the TE displacement data, it was found that a) the camera vibration did not change with wing angle of attack, indicating that it was purely mechanical, and b) when the magnification factor was taken into account the camera displacement did not depend on the lens being used. The camera displacement followed a normal distribution with a mean value of 0μm, a standard deviation of 22μm and a 95% confidence interval of 1μm (for 2000 samples). Expressed in m/s, the 95% confidence interval for the measured velocities due to camera vibration is 0.08m/s, i.e. an order of magnitude smaller than the minimum resolvable velocity, and hence considered negligible. A rigorous description of the quantification of camera displacement can be found in [53].

Sample size effect

For each measurement plane 2000 snapshots were taken. Figure 3 shows the effect of sample size on the measured streamwise velocity for a point inside one of the VG vortices, where flow temporal and spatial variations are stronger, compared to the region outside the vortices. Only the results for the streamwise component are shown since the behaviour of the other components was similar.

In Figure 3, the time averaged streamwise velocity based on the maximum sample size, 2000 snapshots, is drawn as a straight solid line. Above and below this line, two parallel lines are drawn at a distance equal to the minimum resolvable velocity (U_{res} = 0.4m/s, see Appendix). The 95% confidence interval is given with a dashed curved, above and below the time-averaged velocity value. Mean values computed from groups of 100, 250, 500, and 1000 samples are also plotted. For 2000 snapshots, the 95% confidence interval in the most unsteady region of the flow is approximately 0.09 m/s, i.e. an order of magnitude smaller than U_{res}. The corresponding confidence interval for the rms quantities is 6.0%.

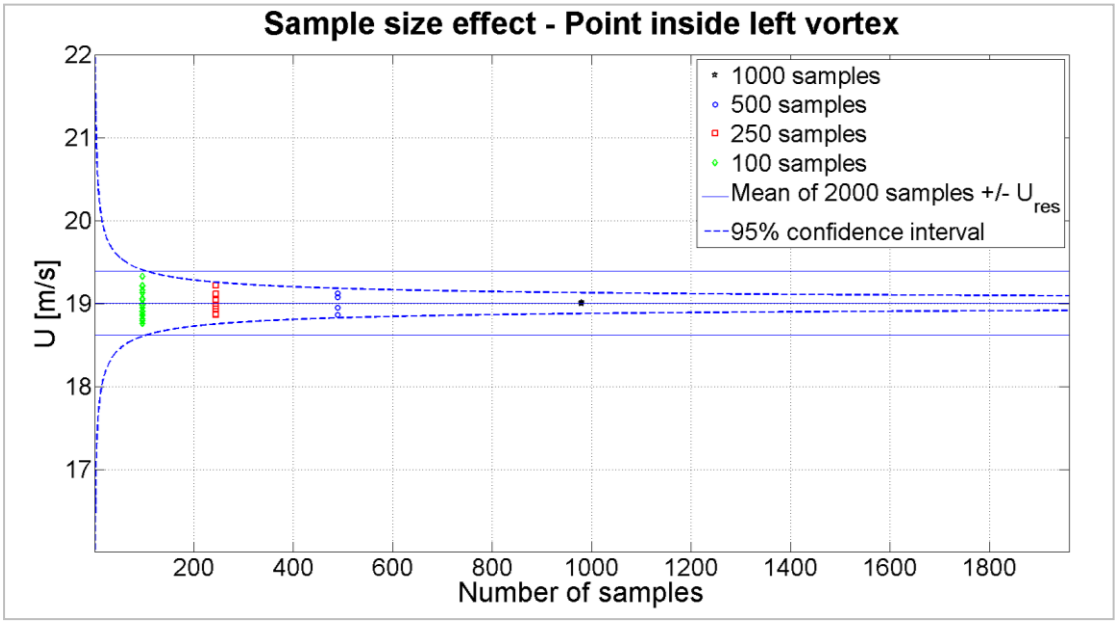

Figure 3: Sample size effect on the streamwise velocity component (U) at a point inside the left vortex. Data from plane C, normal to the flow at x/c = 0.8.

Vortex generator geometry and lay-out

Counter rotating triangular vanes with common flow up were selected as the basic concept of a CFD based parametric investigation [53]. The examined parameters are shown in Figure 4. The best performing VG configuration from that study was investigated experimentally and the results are reported here. The VG height was equal to the local BL thickness, which was δ = 6mm, based on RANS simulations. The details of the selected configuration are given below:

x	=	0.3c	chordwise position of the VG array
β	=	20°	VG angle to the free stream flow
h	=	δ = 6mm	VG height
l	=	3h	VG length
D	=	11.7h	distance between two VG pairs
d	=	3.7h	spanwise distance between the LE of two VGs of the same pair

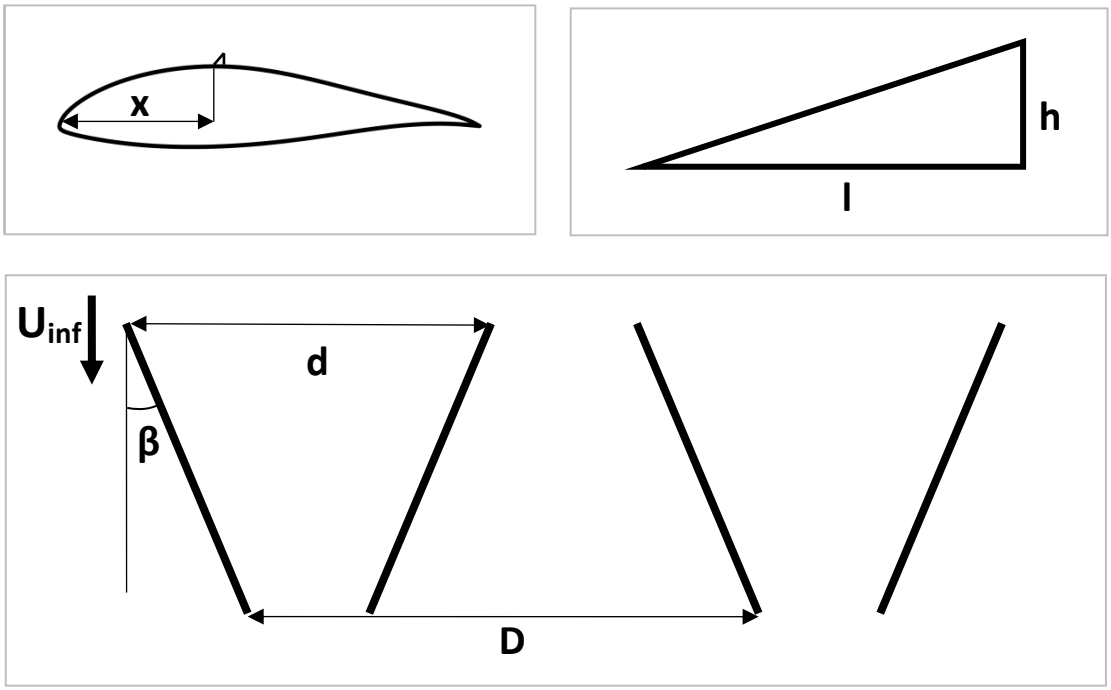

Figure 4: Triangular vane vortex generator parameters: X is the chordwise position of the VG array, l is the VG length, h is the VG height, β is the VG angle with respect to the free stream flow, d is the spanwise distance between the LE of two VGs of the same pair and D is the distance between two VG pairs. U_{inf} in the lower figure indicates the flow direction.

Spatial Resolution

Stereo PIV is a very popular technique for measuring vortex flows [32, 41, 54, 55], but achieving the required spatial resolution can be challenging, especially if steep spatial gradients are involved. In order to sufficiently resolve a vortex flow [56] the ratio of probe size to vortex core radius, α_{RES}, should be:

$$a_{RES} = \frac{L_m}{r_c} < 0.1 \qquad (2)$$

where L_m is the length of the interrogation area and r_c is the vortex radius.

In the present set of experiments this was particularly challenging, given the size of the generated vortices and the camera distance from the measurement planes. Plane A contained the smallest vortices and was furthest away from the cameras. The vortex radius on that plane, defined as the half distance between the two vorticity peaks, was found to be 8mm. To achieve the desired resolution Macro lenses (150mm) and high resolution cameras (4Mpixel) were used. The image deformation technique, as described in [54], was applied to the data. The final interrogation area size was 0.8×0.8 mm, see Table 2.

Velocity derivatives were computed using the least squares approach [57], as given in Eqn. (3). This approximation is second order accurate, cancels out the effect of oversampling and produces smoother results.

$$\left.\frac{dV}{dx}\right|_i = \frac{2V_{i+2} + V_{i+1} - V_{i-1} - 2V_{i-2}}{10\Delta X} \qquad (3)$$

3 Results and discussion

3.1 Pressure measurements

The lift and drag polars are shown in Figure 5 and Figure 6, respectively. The presence of VGs leads to lift enhancement at higher angles of attack. The linear part is extended from α = 6° to α = 11° while maximum lift appears at 16° giving an increase of 0.5 or 44%. A drag penalty of 0.002 was measured for α < 6°. As discussed later on, at 16° the pressure recordings indicate bifurcation of the flow, here denoted by a vertical dotted line.

The pressure distribution at α = 10°, in Figure 7, shows that separation is successfully suppressed. The flow remains attached up to at least x/c = 0.9 and the suction peak is increased. The pressure data at the trailing edge region suggest recovery at higher values, which explains the pressure difference over the pressure side of the airfoil. Pressure perturbations around x = 0.02% in the experimental data are due to the local effect of the ZZ tape on the neighbouring pressure taps.

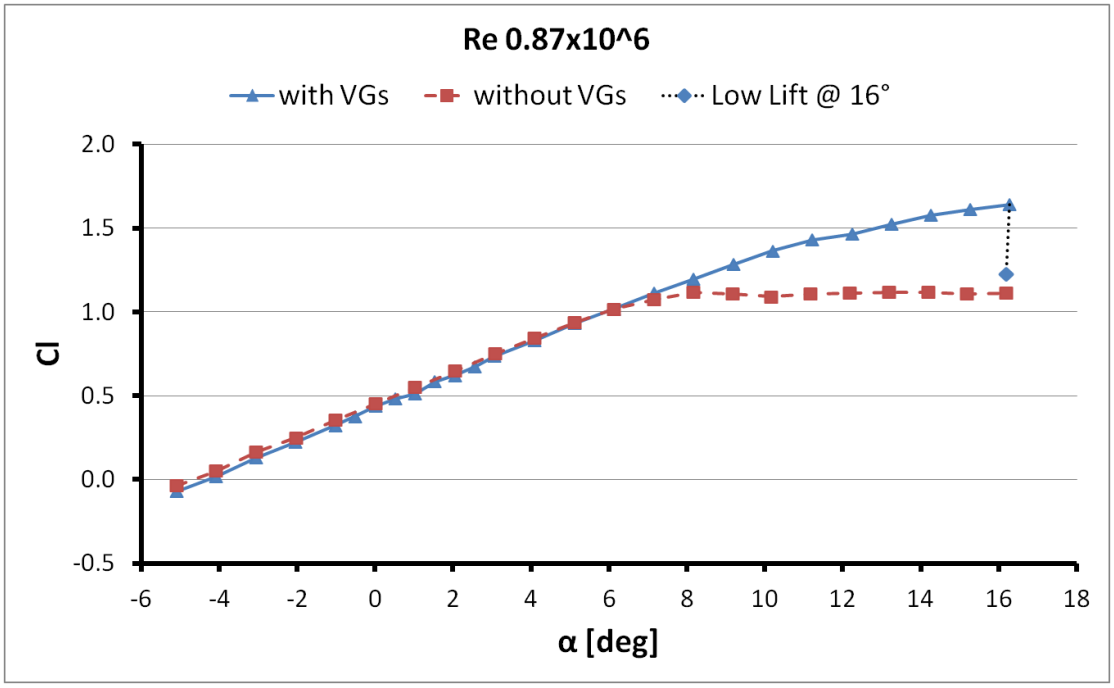

Figure 5: Experimental lift coefficient polar for a wing with and without VGs.

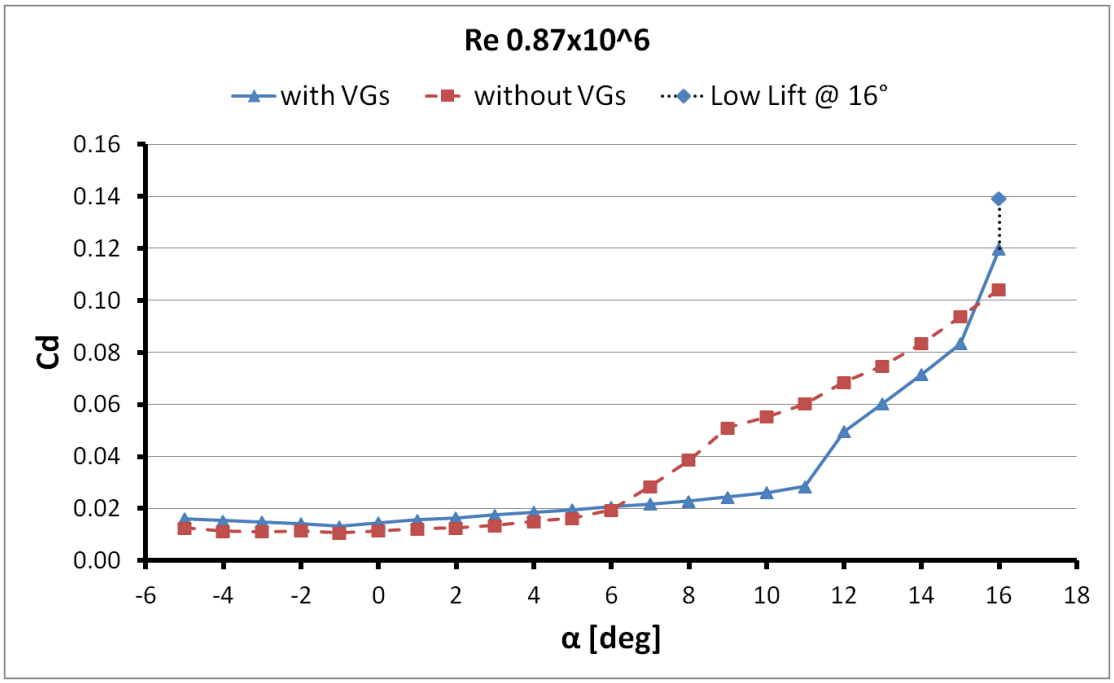

Figure 6: Experimental drag coefficient polar for a wing with and without VGs.

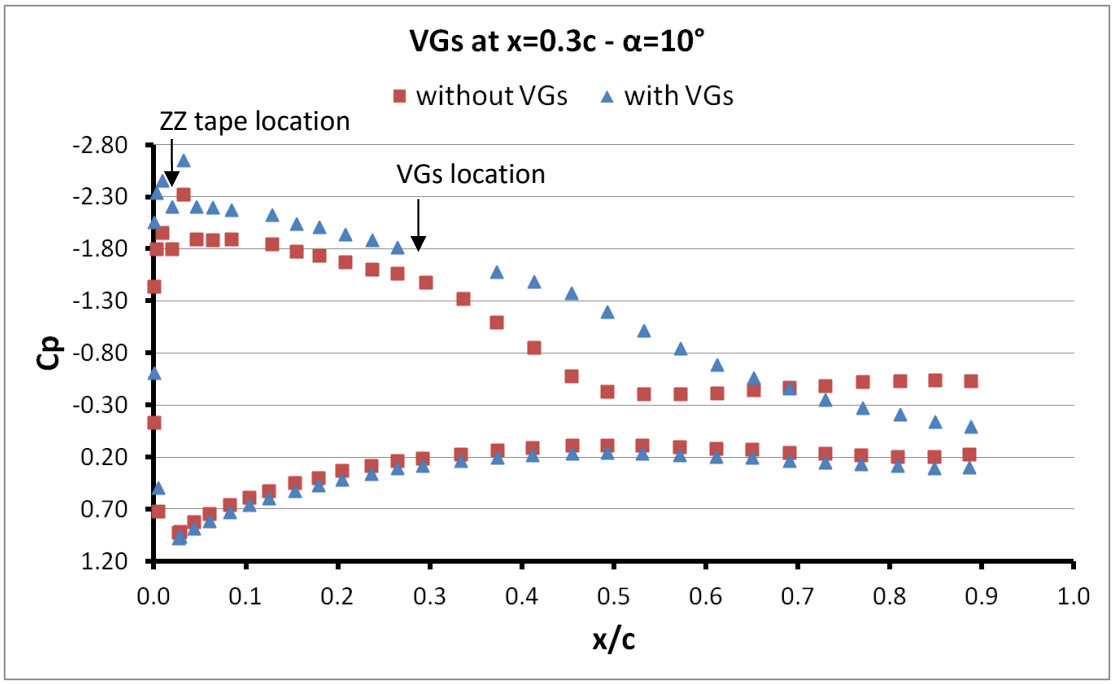

Figure 7: Pressure distribution along the wing chord for a wing with and without VGs at α = 10°.

3.1.1 Bifurcation at 16°

Initially all pressure measurements were taken at 200Hz sampling rate and for 5sec. During the measurements for the controlled case at 16°, however, significant unsteadiness was observed that led to extending the samples to 50sec. No unsteadiness was observed for α < 16°, even when longer samples were taken.

It was found that the flow alternated between two distinct states: a High Lift (HL) state and a Low Lift (LL) state. The HL state, dominated the time series, whereas the less frequent LL

state, would appear for time intervals that would not exceed 3sec. The difference in pressure level between the two states was more pronounced on the suction side, both upstream and downstream of the VGs. As an example, the time series from the suction side pressure tap at x/c = 0.265 is given in Figure 8 (left), clearly showing the two states. The histogram of this measurement is given in Figure 8 (right).

A separate average value for each state was computed resulting in the two pressure distributions shown in Figure 9. The pressure distribution of the uncontrolled case (blue-diamonds curve) is also given for reference. The similarity between the LL state and the uncontrolled case is clear. The HL state is significantly different and the pressure follows the trend found at lower angles, i.e. increased suction peak and limited separation.

The cause of the unsteadiness is not clear. It is possible that the SC causes the destabilization of the VG vortices or that the VG vortices break up due to a different reason allowing the SC to reform. Based on the available data, however, no solid conclusion can be drawn. Simultaneous pressure measurements would be required to obtain a better understanding of the flow. In any case, the onset of such a bifurcation is quite unfavourable, since it would lead to fatigue loads and therefore the operational envelope would have to be reduced.

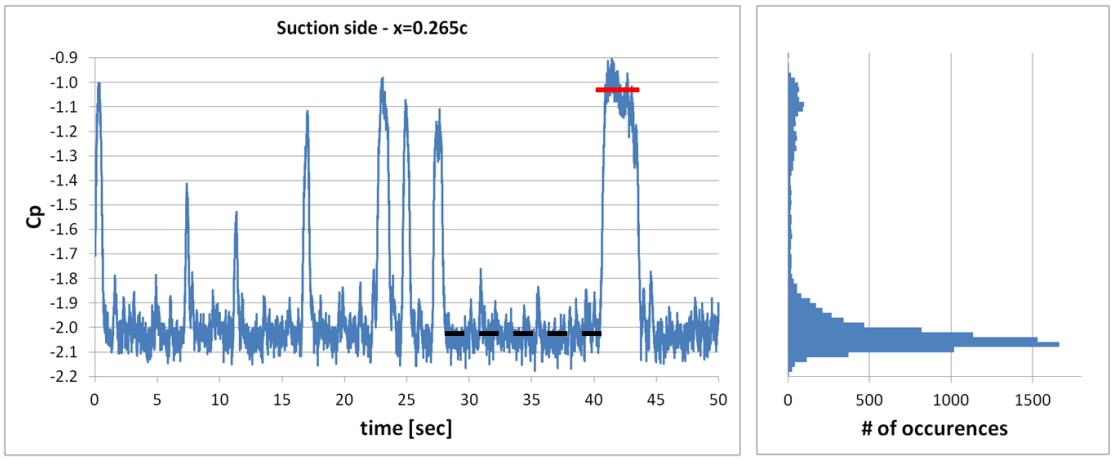

Figure 8: (Left) Time series of pressure measurement taken from the pressure tap on the suction side of the wing located at x/c = 0.265. The states of High (black dashed line at Cp ≈ -2) and Low Lift (red solid line at Cp ≈ -1) are indicated. (Right) Histogram of the same measurement.

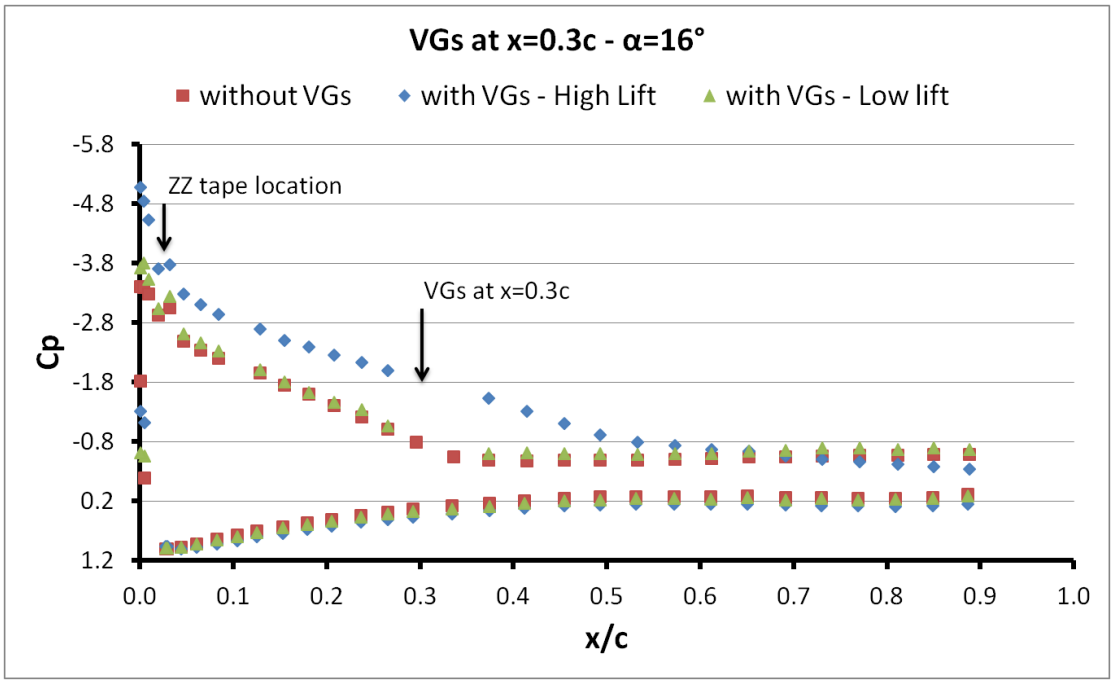

Figure 9: Pressure distribution along the wing chord for a wing with and without VGs. For the case with VGs, the two curves correspond to the High Lift state (blue diamonds) and the Low Lift state (green triangles).

3.2 Oil flow visualization

Figure 10 shows the oil flow pattern on the wing suction side at α = 10°, Re = 0.87×10^6, for the uncontrolled (left) and the controlled case (right). The flow is from left to right and, as the wing is located vertically in the tunnel, gravity affects the final pattern on the wing, dragging the oil mix downwards in areas of low velocity. Only the region for x/c > 0.3 is shown for greater detail.

The SC structure is clearly visible in the uncontrolled case (Figure 10, left). Curve #1 indicates the SC boundary while arrows #2 and #3 show the SC vortex foci. The foci are located at z/S ≈ ±0.13 (the wing mid-span is at z/S = 0). Their chordwise location is x/c ≈ 0.91 and the most upstream point of the SC is at x/c ≈ 0.48. Arrow #4 highlights the tripping effect of the ZZ tape at the centre of the wing span.

Adding the VGs confines separation to x/c ≈ 95% and suppresses SC formation (Figure 10, right). The separation line has a wavy pattern due to the presence of the VG vortices. Part of it is highlighted by the wavy curve #1. The separated region is smaller downstream of the downwash regions (see dashed line #2) and grows downstream of the upwash regions (see dashed line #3). The separated region is also increased downstream of the localised disturbance (see arrow #4). This is expected since the flow is less energetic at this region due to the presence of the ZZ tape. Vortex paths continue all the way to the separated region suggesting that the VG vortices remain close to the wing surface until at least x/c = 0.95.

Three-dimensional corner flow is also apparent at the top (see arrow #5) and bottom (see arrow #6) of Figure 10 (right), where the fences are attached to the wing. The top region appears larger for two reasons; a) gravity drags the oil mix downwards at regions of low velocity and b) the top VG pair distance from the respective fence is greater than that of the

lower one by 1cm and consequently, separation control is more effective at the lower corner.

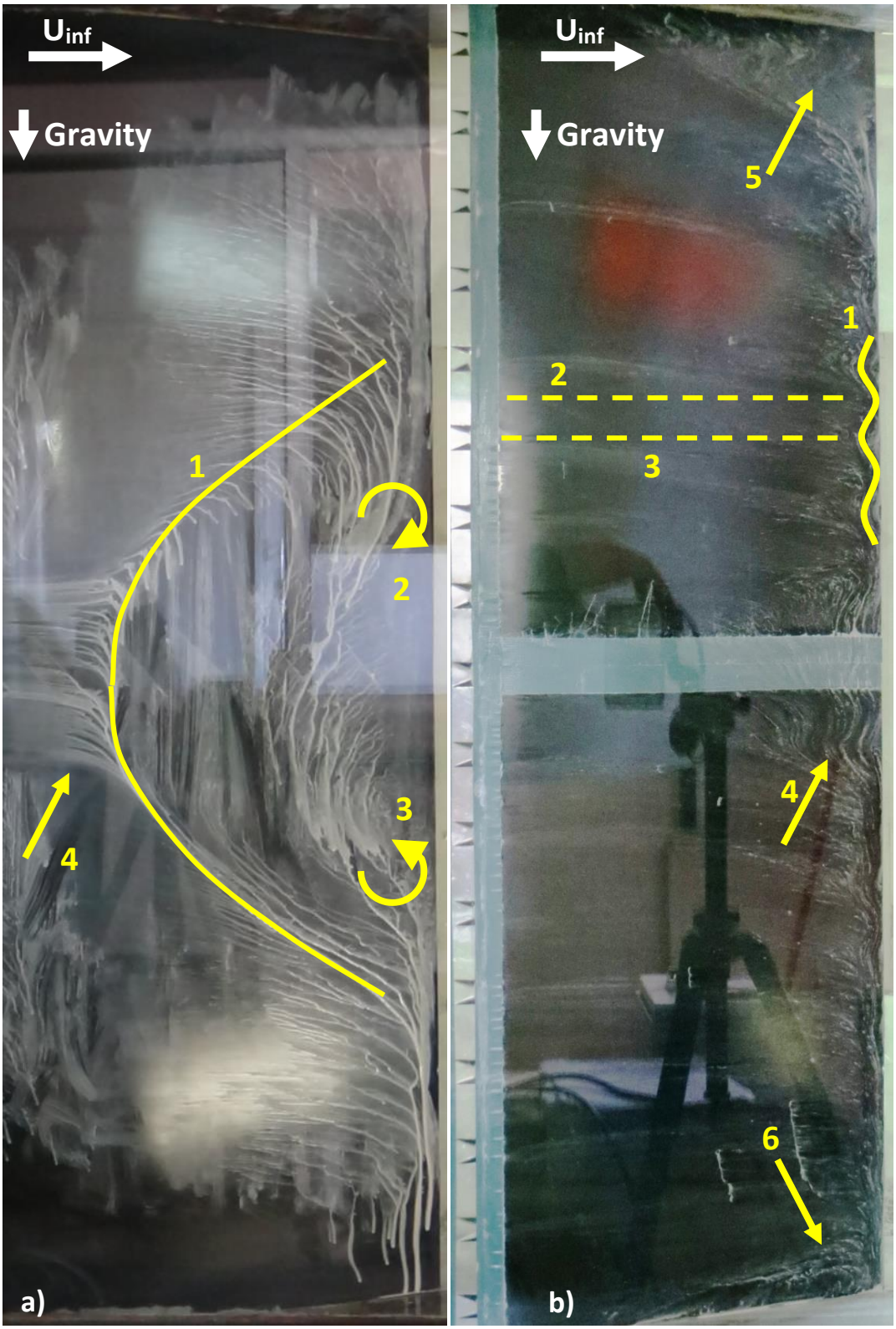

Figure 10: Oil flow visualization for the case without VGs (a) and with VGs (b). Tape (0.2mm high) was used to protect the pressure tapping (at the centre of the wing span) and the VGs during the flow visualization tests.

3.3 Stereo PIV

The analysis of the Stereo PIV data is based on the following indicators/definitions. The position of peak vorticity, ω_{max}, on a plane normal to the flow is considered as the vortex centre and the vortex path is defined by the vortex centre position on the three measurement planes. Circulation is used as a measure of the vortex strength and is computed as the surface integral of vorticity inside the vortex core. There is no consensus regarding the definition of the vortex core [58]. In the present analysis the vortex core is defined as the area around peak vorticity where $\omega_{max} \geq \omega \geq \omega_{lim}$, where $\omega_{lim} = 0.1\omega_{max}$. The vortex core area, $A_{0.1}$, is equal to the area surrounded by the $\omega = \omega_{lim}$ isoline. The "vortex radius", $R_{0.1}$, is equal to the radial distance from the vortex centre to the point where local vorticity is equal to $\omega_{max}/2$. Since the vortex shape is not exactly circular, $R_{0.1}$ was computed using:

$$R_{0.1} = \sqrt{A_{0.1}/\pi} \tag{4}$$

Following Stillfried at al. [59], the vortex velocity field, $V_i(y,z)$, is defined as the difference between the time averaged velocity field, $u_{i,PIV}(y,z) = \overline{u_i(y,z,t)}$, and the mean flow, $U_i(y) = < u_{i,PIV}(y,z) >$. The latter is obtained by spanwise averaging $\langle \quad \rangle$ over the width of the VG pair.

$$V_i(y,z) = u_{i,PIV}(y,z) - U_i(y) \tag{5}$$

3.3.1 Mean flow

Figure 11 compares the normalized profiles of $U_x(y)$ at x/c = 0.6 and x/c = 0.8 for both the controlled and the uncontrolled case (no data were available on plane B for the uncontrolled case [11]). The suppression of separation is confirmed. Furthermore, the flow outside the separated region is accelerated more in the uncontrolled case than in the case with the VGs due to greater boundary layer displacement of the flow.

Figure 12 presents normalized streamwise velocity, $U = u_{x,PIV}/U_{inf}$, and vorticity contours on planes A, B and C along with vorticity isolines of $\omega = \omega_{max}/2$ and vectors of the vortex velocity field, $V_i(y,z)$. On the velocity contours a U isoline is also drawn, indicating the BL height at the sides of the VG pair. The specific value of U corresponds to the U value at the height where $\partial U/\partial y = 0$, at z/h = ±6.

The streamwise velocity shear layer has a distinct Ω shape on plane A, which is subsequently diffused on planes B and C. The VG vortices bring high momentum flow closer to the wing surface and through their combined upwash lift the low momentum flow in the region between them. As discussed later, this mechanism leads to a double peak in the streamwise velocity profile, which is smoothened by diffusion on planes B and C.

Within the Ω region, the two VG vortices are clearly distinguished by the vorticity contours. Their shape on plane A appears stretched in the vertical direction, due to the close proximity of the vortices. Subsequently, the vortex shape changes from plane A to plane B, indicating strong strain, attributed to vortex interaction [24, 33]. This effect appears to diminish further

downstream, as the contour shapes on planes B and C are similar to each other suggesting that diffusion dominates over this part of the flow. The locations of peak vorticity (shown as black marks in Figure 12) are always at the lower part of the vorticity contours.

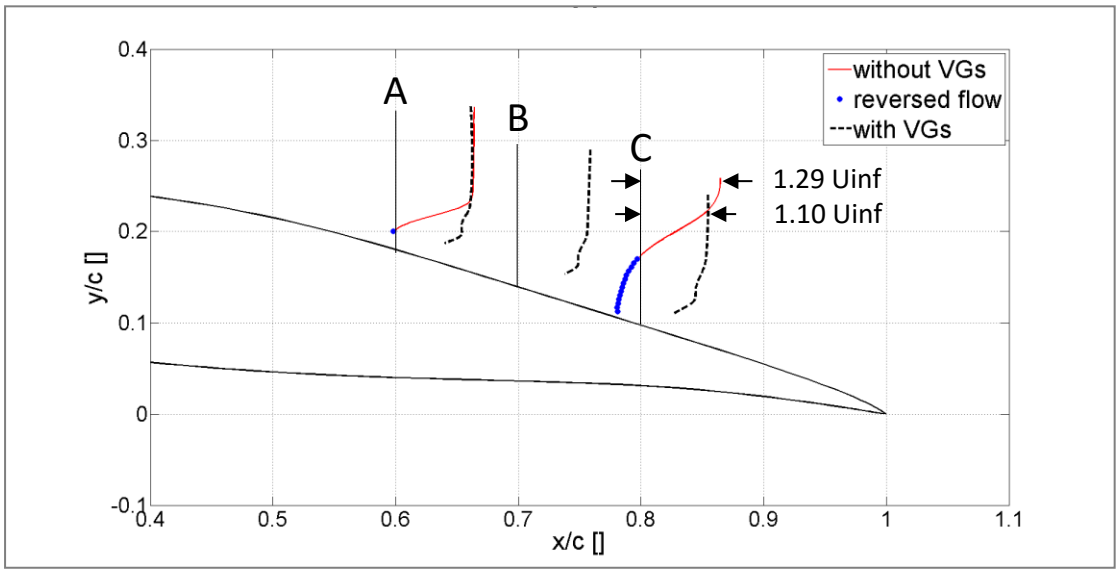

Figure 11: Normalized streamwise velocity profiles at streamwise locations x/c = 0.6, x/c = 0.7, x/c = 0.8. For the uncontrolled case the profile at the centre of the wing span is plotted and negative streamwise velocity values are shown with blue circles. For the controlled case the streamwise component of the mean flow, $U_x(y)$, is plotted. For the uncontrolled case, no data were available at x/c = 0.7.

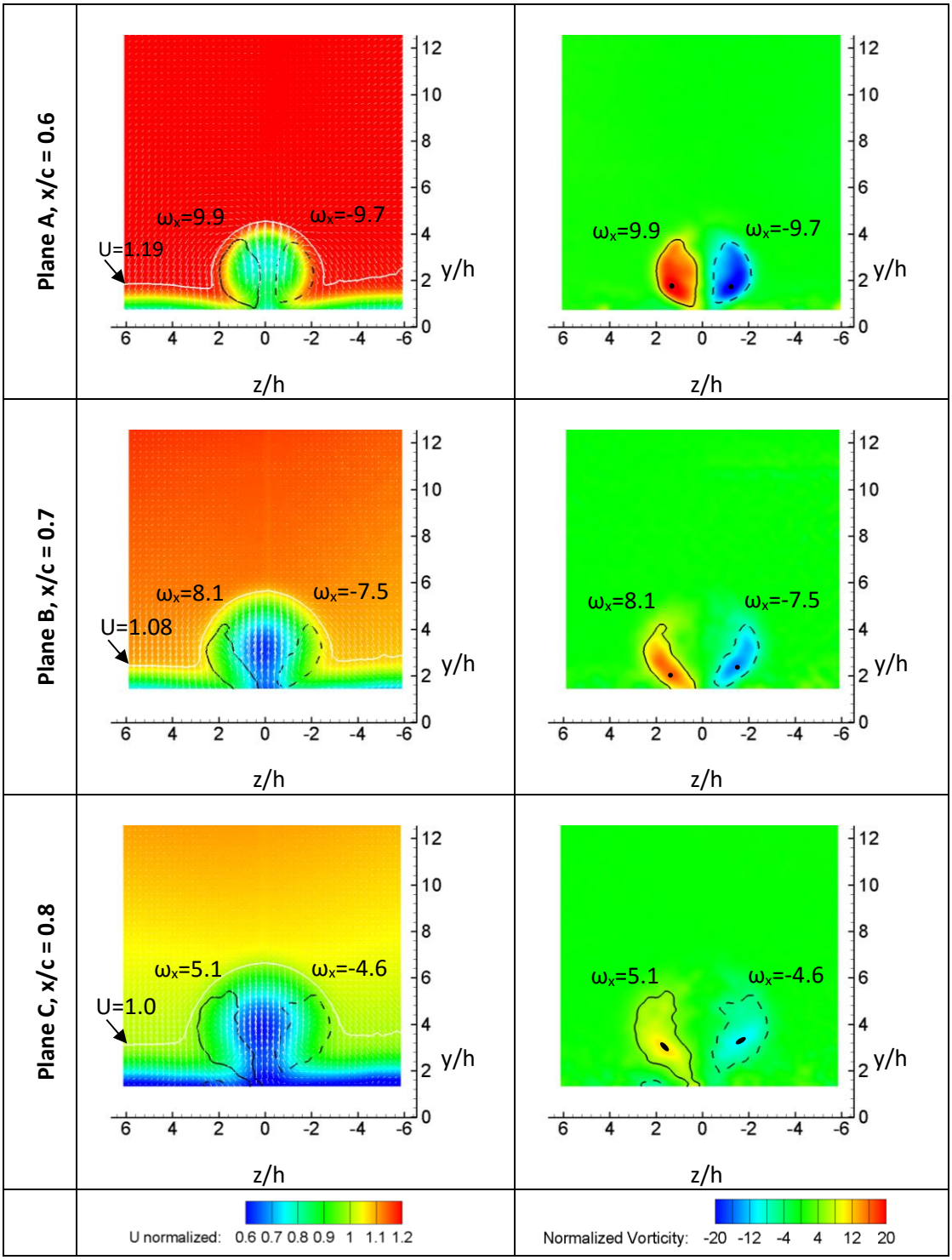

Figure 12: (Left Column) Normalized streamwise velocity contours and vectors of the in plane vortex velocity field. One out of every four vectors is plotted for clarity. The solid white line is a U isoline, at the height where $\partial U/\partial y = 0$, at $z/h = \pm 6$. (Right Column) Normalized vorticity contours. Vorticity isolines $\omega = \omega_{max}/2$ for each vortex are also plotted. Top, middle and bottom rows correspond to planes A ($x/c = 0.6$, $\Delta x/h = 27.2$), B ($x/c = 0.7$, $\Delta x/h = 37.2$) and C ($x/c = 0.8$, $\Delta x/h = 47.2$), respectively. Vorticity peak locations are indicated by black marks. The wing surface is always at $y/h = 0$ and $z/h = 0$ is the centreline between the two VGs.

Vortex Path

The vortex centre location on all measured planes is given in Figure 13 (left). It is observed that vortices move away from each other and away from the wing surface as they proceed downstream. On plane A (x/c = 0.6 or 27.2 heights downstream of the VG TE), the vortex centre is at 1.6h above the wing, indicating limited vortex displacement in the vertical direction since their formation. On the other hand, the vortex centre distance from the wing surface almost doubles from plane A to plane C. This cannot be attributed to vortex core growth since, as it will be shown, the vortex radius has only grown ~30% over the same distance. Conceivably the vortex cores are displaced in the vertical direction due mutual induction/upwash and surface curvature.

The right vortex centre appears to be higher than the left vortex centre on planes B and C. This could be attributed to vortex interaction, since the left vortex, and hence its effect, is stronger than the right one (see vorticity isolines in Figure 12). The difference in vortex strength is attributed to inaccuracies in the VG construction. The right hand side VG was measured to be 0.5mm shorter and at ~1° lower angle with respect to the free stream than the left VG.

Vortex Size

The evolution of the vortex size is shown in Figure 13 (right) where the evolution of $R_{0.1}$ is plotted. A linear growth of $R_{0.1}$ is observed throughout the measurement range. Attention is drawn to the fact that, while $R_{0.1}$ grows at an almost constant rate, the vortex shape changes from plane A to plane B (due to shear on the yz plane, as discussed later), whereas it is simply diffused from plane B to plane C.

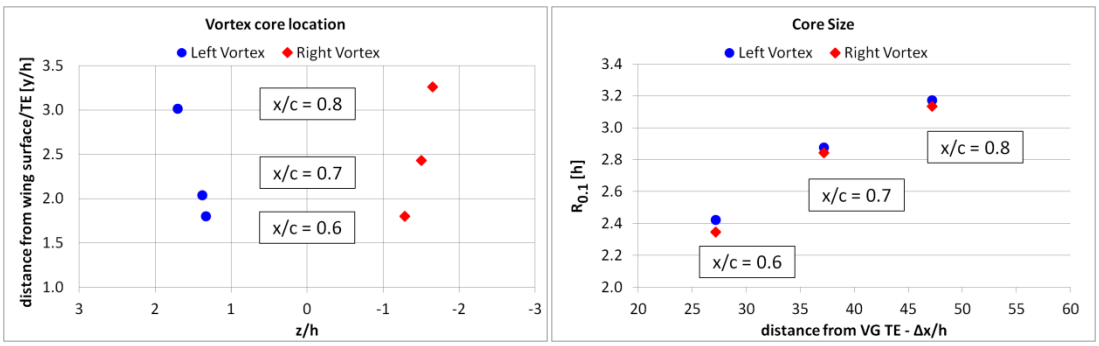

Figure 13: (Left) Vortex centre location on the XZ plane and (Right) "Vortex radius" at the three measurement planes.

Vortex Strength

Vortex circulation and peak vorticity on all measurement planes for both vortices are plotted in Figure 14. In order to examine the downstream decay of vorticity, both quantities are normalized by their respective values on plane A. The drop in circulation approaches the exponential decay suggested by LöGdberg et al. [19] for counter rotating vortices generated by low-profile VGs on a flat plate flow under zero pressure gradient. Peak vorticity drops at a higher rate in comparison to circulation, as expected.

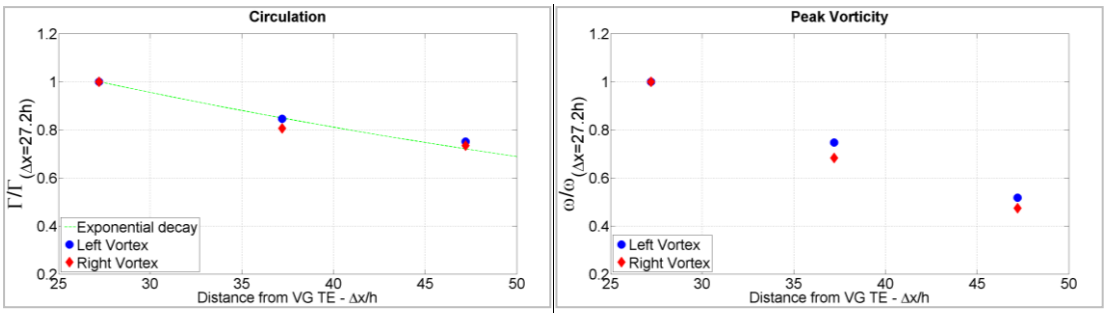

Figure 14: (Left) Vortex circulation and (Right) absolute peak vorticity at the three measurement planes. Both quantities are normalized by their respective values on plane A. On the circulation graph the exponential decay suggested in [19] is also shown.

3.3.2 Turbulence characteristics

In this section the measured Re stresses $\overline{u_i'u_j'}$ (negative sign not included) are presented along with computed Re stress production terms and turbulent kinetic energy.

The discussion on the downstream evolution of the VG vortices indentifies the following mechanisms. The early stage is dominated by strong turbulent momentum transport across: a) the Ω-shaped shear layer, as signified by high values of $\partial U/\partial y$ and $\partial U/\partial z$, and b) between the two vortices. Further downstream, diffusion takes over resulting in smoother distributions of the various turbulence quantities with reduced peak values. Regions of high normal stresses in all directions are related to strong velocity gradients. However, excessively high values of $\overline{v'v'}$ between the two vortices are attributed to vortex wandering, which adds to turbulence production.

Reynolds Stresses distribution

On plane A (Figure 15, top row), regions of high $\overline{u'u'}$ values unsurprisingly follow the shape of the streamwise velocity shear layer, (see also Figure 12). An area of high $\overline{v'v'}$ is formed at the top region between the two vortices, with values higher than those of the other normal stresses. Symmetric peaks of $\overline{w'w'}$ on the two sides of the z = 0 plane are observed, in agreement with [33, 35]. In [35] these peaks were linked to vortex wandering.

Indication of vortex wandering was found in the measurement snapshots. They confirm that the vortices move at times independently in the spanwise direction (towards or away from each other) and at times as a pair, in the positive or negative Z direction. When the two vortices approach each other, the combined upwash between them becomes strong, whereas it is weakened when they move away from each other. Such a movement could explain the high $\overline{v'v'}$ values at the top region. The $\overline{v'v'}$ peak above the two vortices at the region of outflow was also observed in [21], where the case of counter rotating vortices in an adverse pressure gradient BL flow was studied.

Moving to plane B, at x/c = 0.7, the shape of $\overline{u'u'}$ and $\overline{v'v'}$ distributions retains its form but peak values are now reduced and their spatial distribution diffused. Values of $\overline{v'v'}$ are no longer the highest amongst the normal Re stresses, which are now comparable in magnitude between them. Unlike the other normal stresses, $\overline{w'w'}$ distribution has changed: the two symmetric peaks give place to a smaller peak in the region of upwash between the two vortices. As shown later, this is not due to production of $\overline{w'w'}$, but conceivably due to convection of the normal stress.

Finally, on plane C normal Re stress distributions are similar to those on plane B, supporting the view that between these two planes diffusion takes over as the main flow mechanism. On the contrary, the difference in Re stress distributions between plane A and B suggests that, in that region, vortex interaction and turbulent transport of momentum between the vortices and the underlying flow is still strong.

Contours of the shear Re stresses on all planes are given in Figure 16. Shear stresses levels are one order of magnitude smaller than the normal stresses levels. Starting again with plane A, negative $\overline{u'v'}$ values follow the top part of the Ω-shaped shear layer while along the outer part of the same shear layer $\overline{v'w'}$ takes over. Positive $\overline{u'v'}$ values at approximately z/h = ±1, also follow the shape of the shear layer, but change sign due to its orientation. Both $\overline{u'w'}$ and $\overline{v'w'}$ have antisymmetric distributions, as expected. The high values of $\overline{v'w'}$ at the top of the two vortices indicate regions of strong shear on the yz plane. The overall structure is similar to the results presented in [33].

Further downstream, on plane B, the region of negative $\overline{u'v'}$ that bridges the two vortices has grown, while positive values are hardly visible as the shape of the streamwise velocity shear layer is now smoothened. Also, $\overline{u'w'}$ contours are significantly diffused. The vortex shape has changed mainly at the top part, where the concentration of $\overline{v'w'}$ is now smaller. Regions of high $\overline{v'w'}$ values are now concentrated inside the vortices indicating the end of strong turbulent transport across the outer shear layer of the vortex pair. Contours on plane C are very similar to those on plane B, only more diffused.

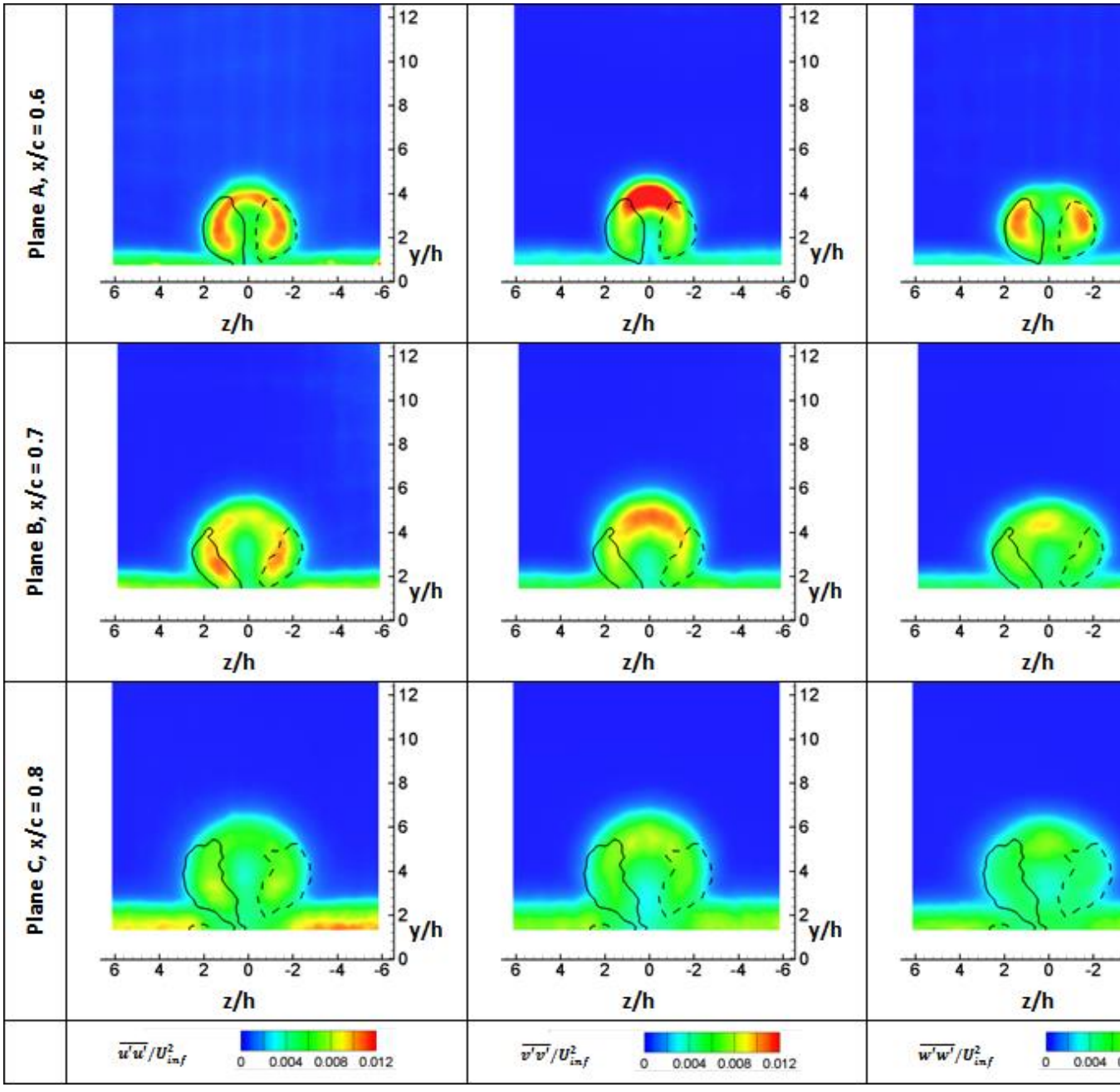
Plane A, x/c = 0.6
Plane B, x/c = 0.7
Plane C, x/c = 0.8
y/h
z/h
12
10
8
6
4
2
0
6
4
2
0
-2
-4
-6
$\overline{u'u'}/U_{inf}^2$
$\overline{v'v'}/U_{inf}^2$
$\overline{w'w'}/U_{inf}^2$
0
0.004
0.008
0.012

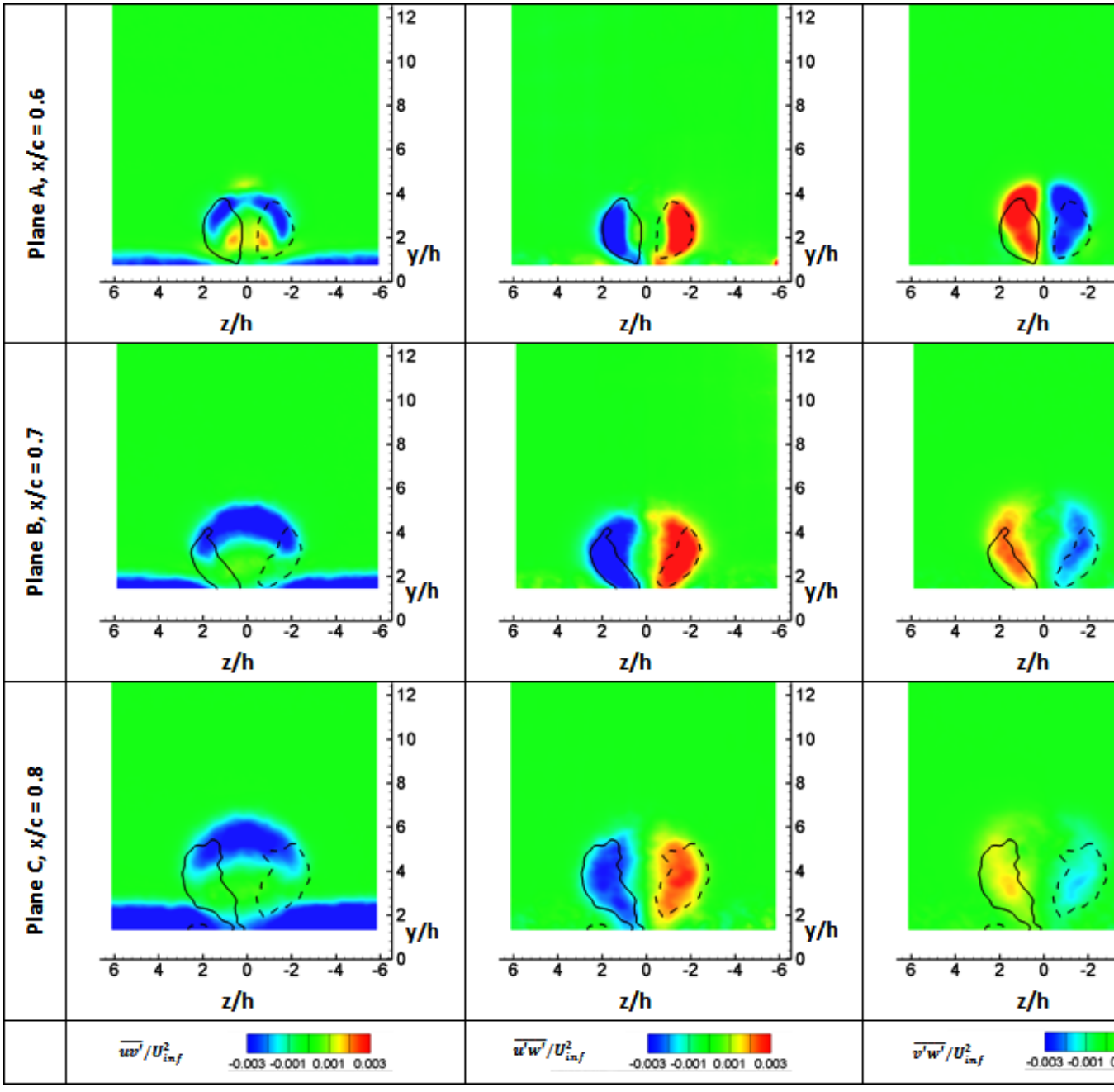
Plane A, x/c = 0.6
Plane B, x/c = 0.7
Plane C, x/c = 0.8
y/h
z/h
12
10
8
6
4
2
0
6
4
2
0
-2
-4
-6
$\overline{uv'}/U_{inf}^2$
$\overline{u'w'}/U_{inf}^2$
$\overline{v'w'}/U_{inf}^2$
-0.003 -0.001 0.001 0.003

Relation to time averaged flow gradients

In order to examine the relation between the time averaged velocity gradients, the Re stress production and the Re stresses themselves, their variation along vertical and horizontal lines is presented and discussed. The lines are shown graphically in Figure 17 and their exact positions are given in Table 3. Figure 17 also shows contours of the vertical ($V = u_{y,PIV}/U_{inf}$) and spanwise ($W = u_{z,PIV}/U_{inf}$) time averaged flow components for reference. Figures from 18 to 20 refer to the vertical lines j1, j2 and j3 while figures from 21 to 23 refer to the horizontal lines i1, i2 and i3. The vertical lines are all taken on the left hand side (LHS) of the measurement planes, since conclusions from the right hand side are the same. All figures give the $U = u_{x,PIV}/U_{inf}$ profile along with $\partial U/\partial y$ and $\partial U/\partial z$ side by side with the turbulent kinetic energy (TKE), the normal and shear Re stresses and their production terms, $P_{u_i u_j}$:

$$P_{u_i u_j} = -\overline{u_i' u_k'}\frac{\partial U_j}{\partial x_k} - \overline{u_j' u_k'}\frac{\partial U_i}{\partial x_k} \tag{6}$$

In Eqn. (6), the x derivatives of the time averaged flow are considered small in comparison to the vertical and spanwise variations and are therefore omitted.

Plane		A	B	C
Chordwise position (x/c)		0.6	0.7	0.8
Distance form VG TE ((x-x_{VG})/h)		27.2	37.2	47.2
Vertical lines spanwise location (z/h)	j1, *"between the two vortices"*	0.0	0.0	0.0
	j2, "*through the vortex centres*"	1.3	1.5	1.7
	j3, "*left of the LHS vortex*"	2.6	3.0	3.4
Horizontal lines distance from the wing surface (y/h)	i1, "*top part of the BL*"	1.0	1.8	2.4
	i2, "*through the vortices*"	1.8	2.3	3.1
	i3, "*top part of the vortex pair*"	3.9	5.0	6.4

Table 3: Details of the lines along which data are plotted in Figure 18 to Figure 23

Starting with line j1 placed in between the two vortices, Figure 18, the U profile is found to have double peaks, on all planes. This is due to the high velocity fluid entrained by the VG vortices inside the boundary layer. The upper part of the flow, i.e. the region higher than the lower U peak, is dominated by the strong peak in $\partial U/\partial y$, which is also present in all three planes. TKE, P_{vv}, P_{uv}, $\overline{v'v'}$ and $\overline{u'v'}$ also peak at maximum $\partial U/\partial y$ in agreement with [21] where the effect of streamwise vortices on a separating BL was studied.

In plane A, P_{vv} is the highest normal stress production term. This is due to vortex wandering as explained earlier. In planes B and C, on the other hand, where diffusion becomes dominant, P_{uu} and P_{vv} are comparable. In the region of peak $\partial U/\partial y$, negative P_{ww} is connected to locally positive $\partial W/\partial z$ (not shown here for the sake of readability of the plots). Limited $\partial U/\partial z$ deviations from zero at the line between the two VGs are attributed to the VG model asymmetry.

As the curved wing surface is approached on plane A, i.e. at positions lower than the first U peak, not only $\overline{v'v'}$ but also $\overline{u'u'}$ tend to zero faster than $\overline{w'w'}$, while in the next two planes a rather balanced distribution is observed. Relatively high values of $\overline{w'w'}$ appear at the top

part of the BL on planes B and C, while the relevant production terms and the gradients of W (not shown here) in this region remain negligible. Therefore, this activity could be attributed to convection. Negative P_{vv} on plane A is connected to the inflection point in the U profile.

Along line j2 (passing through the vortex centre, Figure 19), both U gradients are significant. P_{vv} and P_{uv} as well as the corresponding Re stresses remain correlated to $\partial U/\partial y$ on all measured planes. This is in agreement with [20] where the velocity deficit was found to have an important effect on the distribution of $\overline{u'v'}$ within the vortex core. TKE, $\overline{u'u'}$ and $\overline{w'w'}$ appear correlated to $\partial U/\partial z$ at this station, in agreement with [21]. P_{vw} and $\overline{v'w'}$ follow the variation of $\partial V/\partial z$ (not shown here). An indication on the variation of V and W on all planes can be drawn from Figure 17 contours.

On the left side of the LHS vortex (line j3, Figure 20), the flow is less affected by the three-dimensionality of the vortical flow and the Re stress distribution resembles that of a turbulent BL [60]. There is indication of the presence of the VG vortices in the U profile, which is associated to the small bump in the k distribution (indicated by vectors in Figure 20). All activity is within y/h < 3. $\partial U/\partial y$ is strong and combined with strong but balanced normal Re stresses and negative $\overline{u'v'}$ Re stress. The variation in $\partial U/\partial z$ values is close to zero and the same holds for the corresponding production terms.

Figure 21 shows the variation of the turbulence quantities along the horizontal line i1, located inside the BL. The vertical position of line i1 is defined by the height at which the local streamwise velocity at the sides of the Ω-shaped BL is ~0.8 times the local free stream velocity. The graphs show that outside the area that is affected by the vortices, P_{uv} is negative and P_{ww} is practically zero, as expected in a turbulent BL. P_{vv} on the other hand, takes positive values due to surface curvature. P_{vv} is reduced in the vortex region due to an increase in $\partial V/\partial y$ (not shown here) and P_{uv} tends to zero as $\partial U/\partial y$ decreases. The normal stresses peak at the location of the strongest velocity shear of their respective velocity components in agreement with [19] while they remain comparable in magnitude. On all planes, $\overline{u'w'}$ and P_{uw} show strong negative correlation with $\partial U/\partial z$, in agreement with [21]. In comparison to the profiles at a greater distance from the wing surface (line i2, Figure 22 and line i3, Figure 23), data from inside the BL are more noisy and the effect from the vortices is not as pronounced.

Moving higher from the wing surface along the horizontal line passing through the vortex centres (line i2, Figure 22) the correlation between P_{uu}, P_{uw} and the respective Re stresses with $\partial U/\partial z$ is still strong. Also, P_{uv} negatively correlates with $\partial U/\partial y$ especially on plane A. By comparing the shear stress distributions on the three planes, it follows that changes in shape are found between the first two planes while between planes B and C the shear stress profiles are basically smoothened, indicating once more the dominance of diffusion.

At the top of the vortex pair (line i3, Figure 23), on plane A, production is dominated by high values of P_{vv} and P_{uv}, both correlated to $\partial U/\partial y$. Normal Re stress $\overline{v'v'}$ is also very strong following P_{vv}. This is attributed to the spanwise wandering of the vortices as already discussed. The negative correlation of $\partial U/\partial y$ with $\overline{u'v'}$ is related to turbulent transport through the U shear layer. On plane B, P_{vv} and P_{uu} are comparable and the contribution of the normal stresses to TKE more balanced. On all three planes, P_{uw} follows $\partial U/\partial z$ while P_{vw}

follows $\partial V/\partial z$ (not shown here). As in the previous horizontal lines, passage from plane B to C is dominated by diffusion.

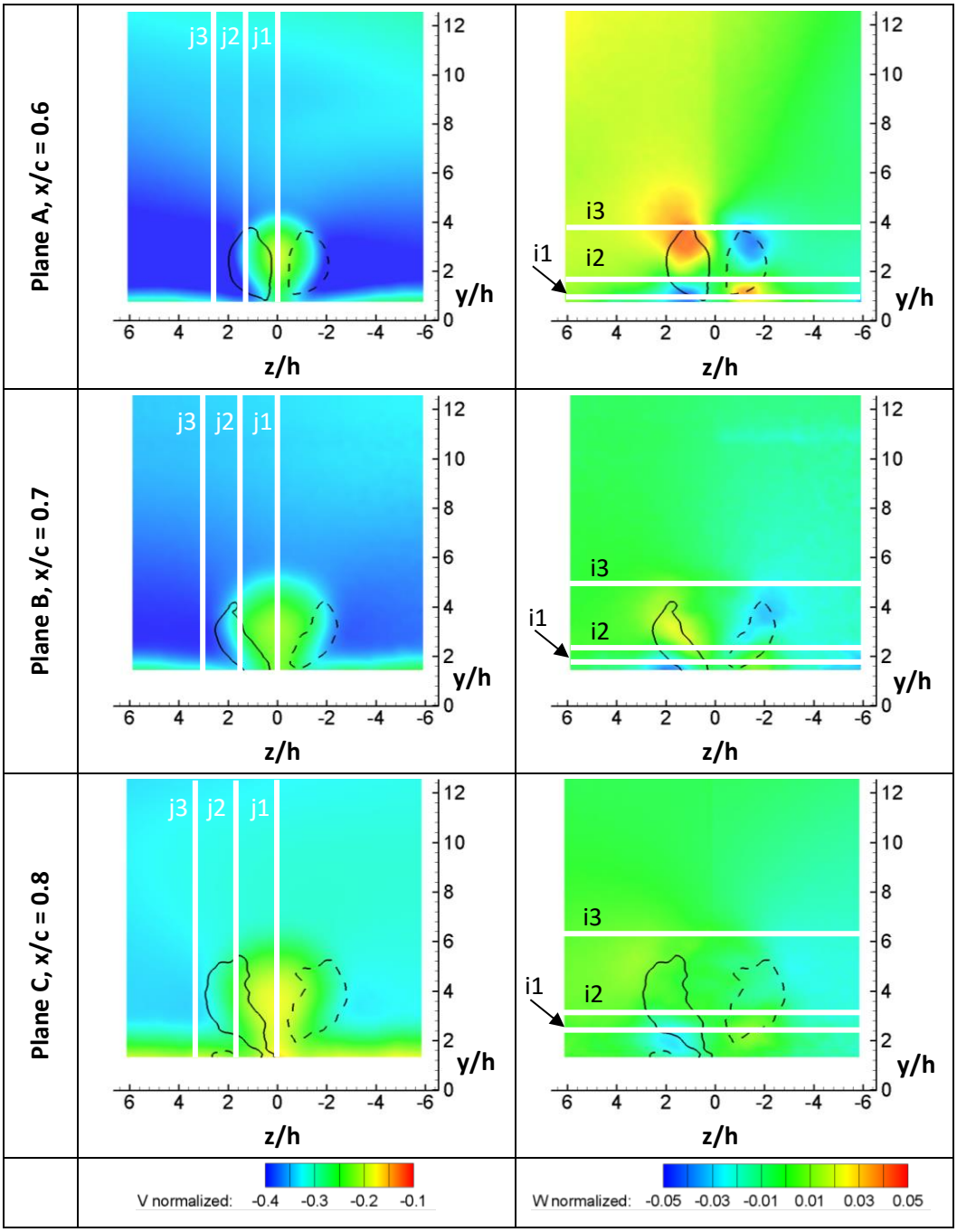

Figure 17: (Left Column) Normalized vertical velocity (V) contours. (Right Column) Normalized spanwise velocity (W) contours. Vorticity isolines for ω = ω_{max}/2 for each vortex are also plotted. Top, middle and bottom row correspond to planes A (x/c = 0.6 or Δx/h = 27.2), B (x/c = 0.7 or Δx/h = 37.2) and C (x/c = 0.8 or Δx/h = 47.2), respectively. The wing surface is always at y/h = 0 and z/h = 0 is the centreline between the two VGs. Thick white cuts indicate the lines along which data are plotted in Figure 18 to Figure 23. The exact positions of the lines/cuts are given in Table 3.

	Between the two vortices (centre of the VG pair)		
Plane A, x/c = 0.6	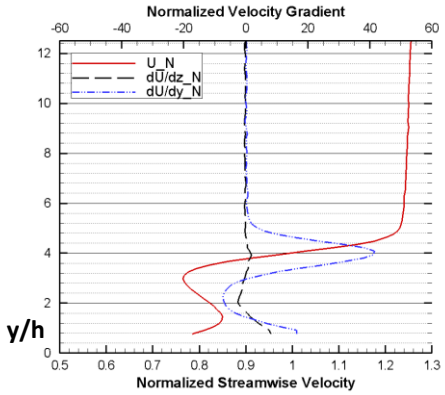	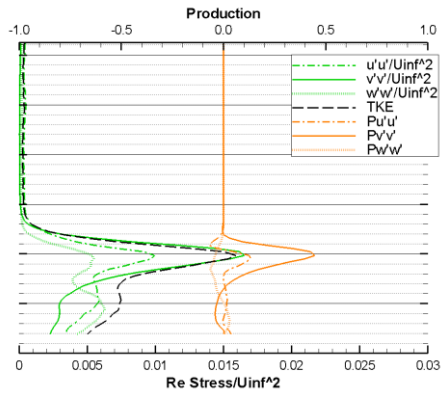	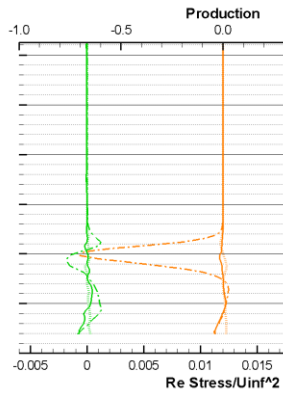
Plane B, x/c = 0.7	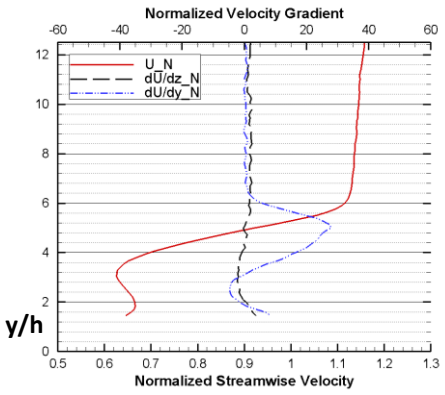	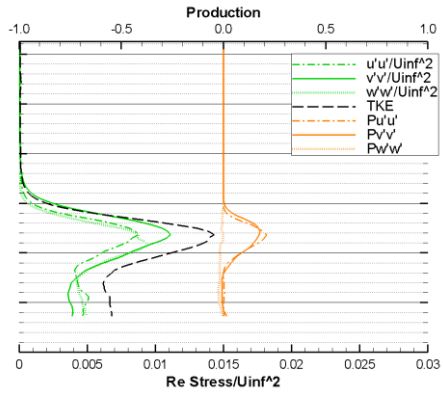	
Plane C, x/c = 0.8	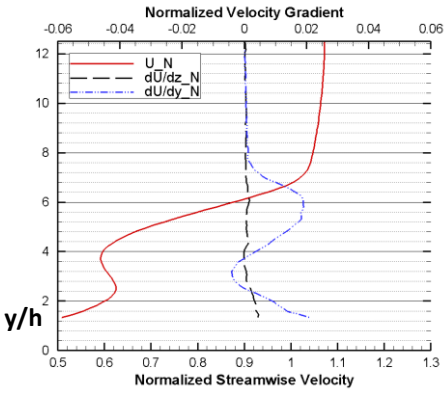	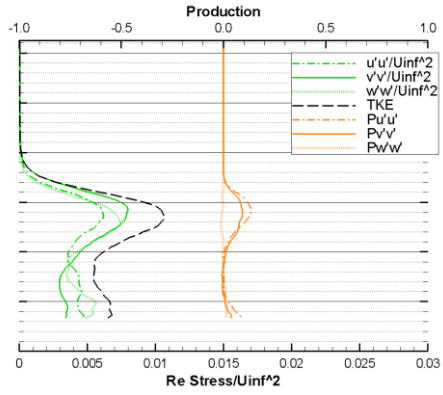	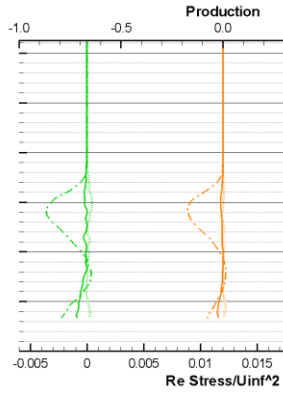

	Through the LHS vortex centre		
Plane A, x/c = 0.6	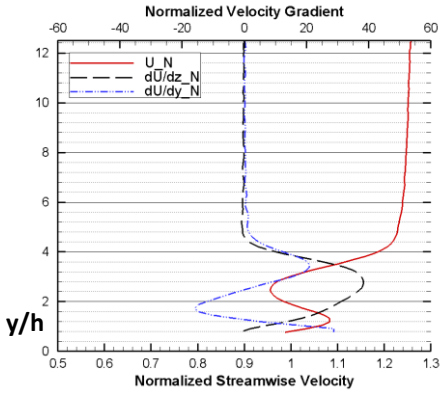	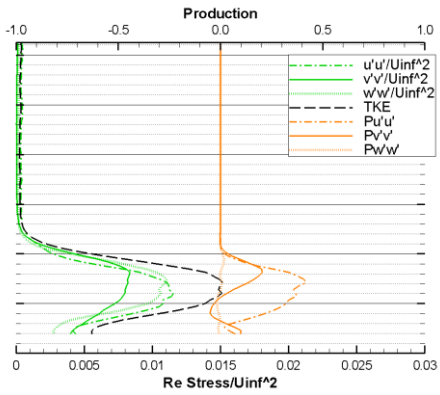	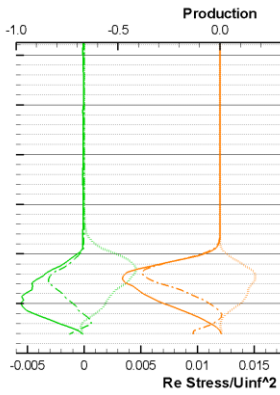
Plane B, x/c = 0.7	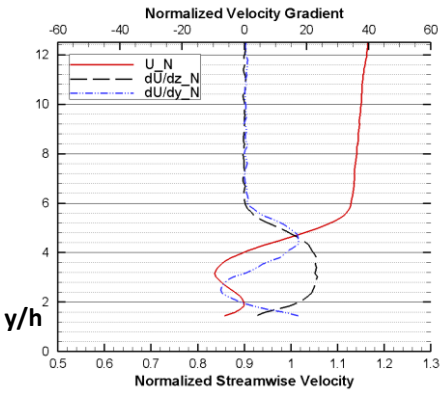	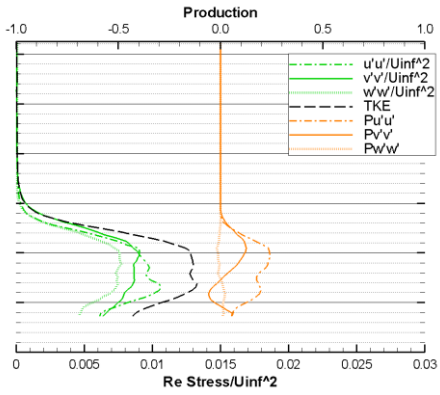	
Plane C, x/c = 0.8	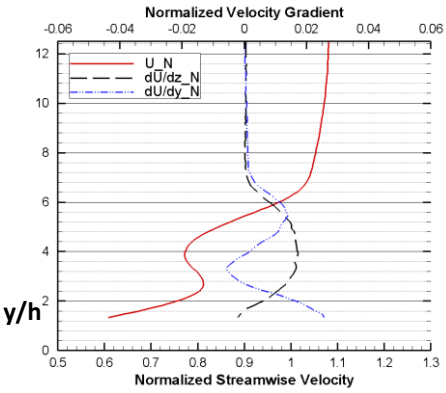	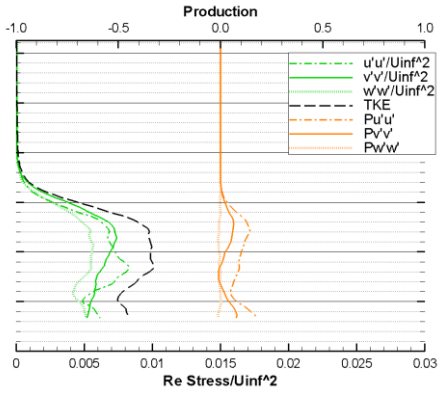	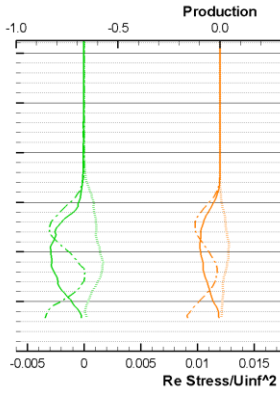

	At the side of the LHS vortex		
Plane A, x/c = 0.6	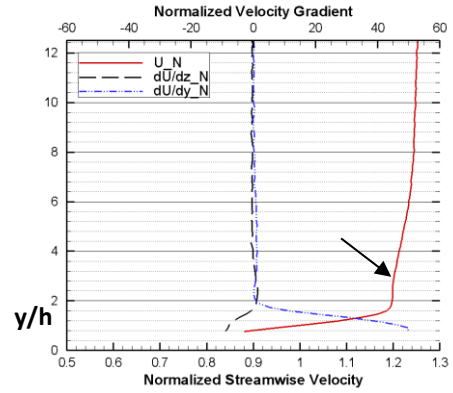	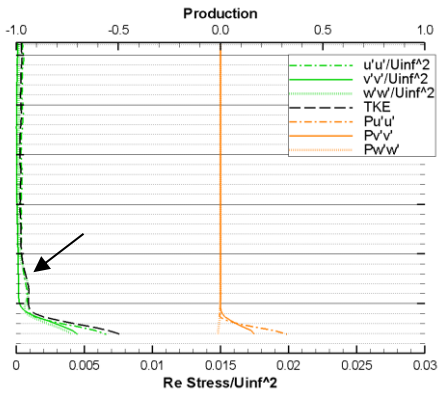	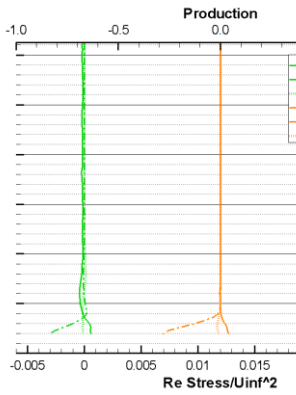
Plane B, x/c = 0.7	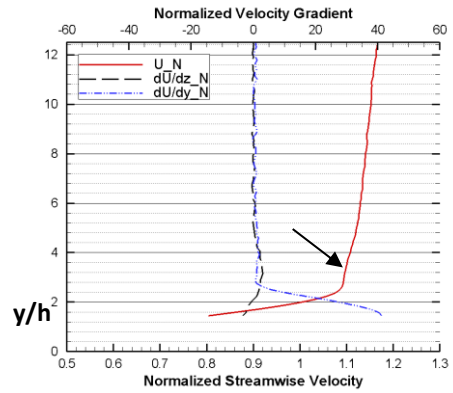	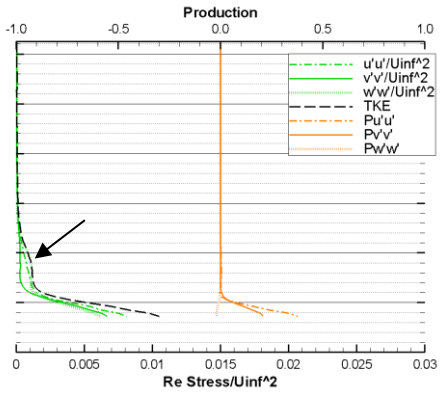	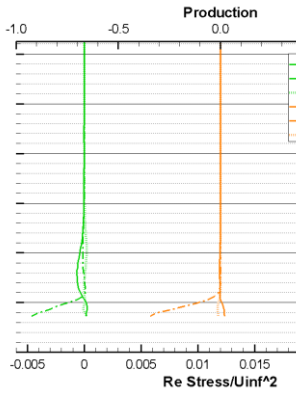
Plane C, x/c = 0.8	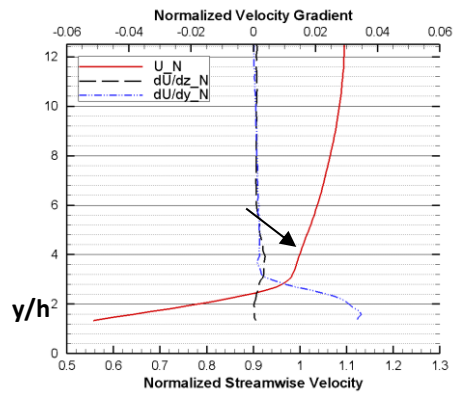	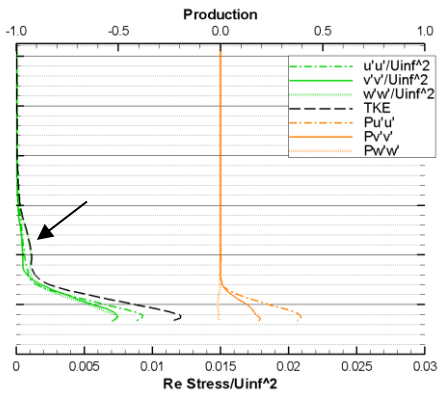	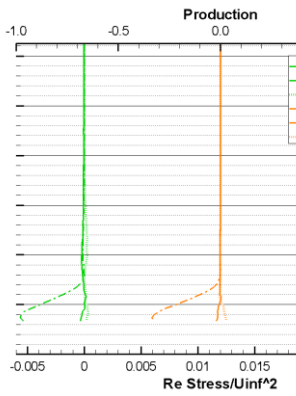

	Top part of the BL		
Plane A, x/c = 0.6	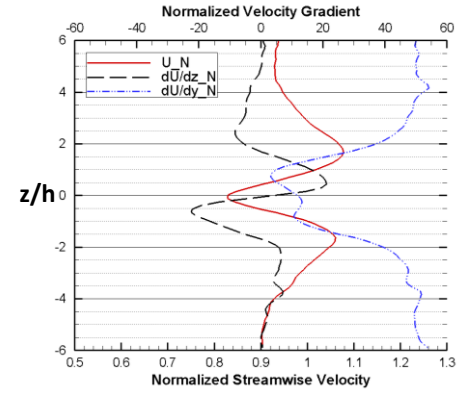	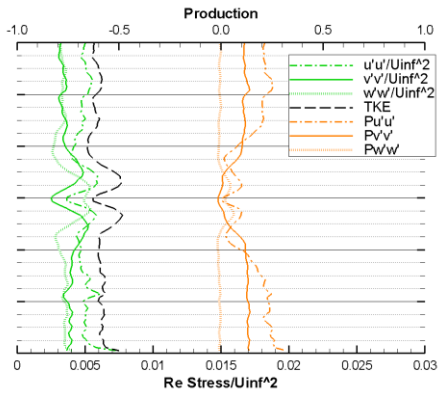	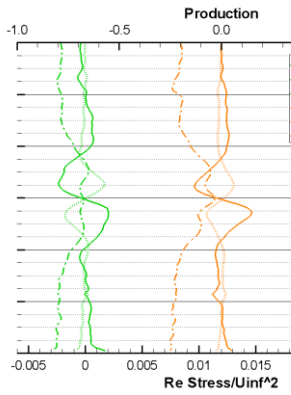
Plane B, x/c = 0.7	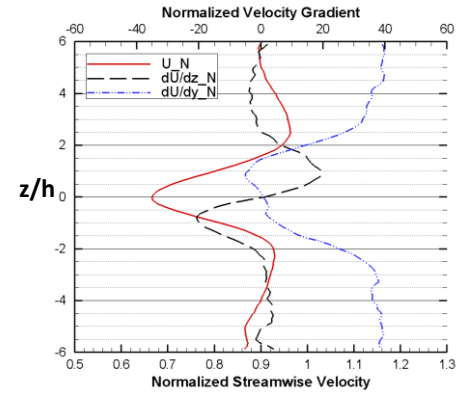	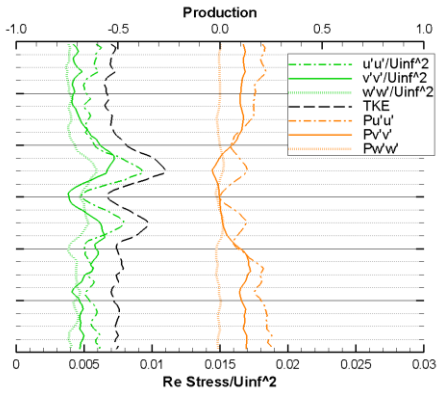	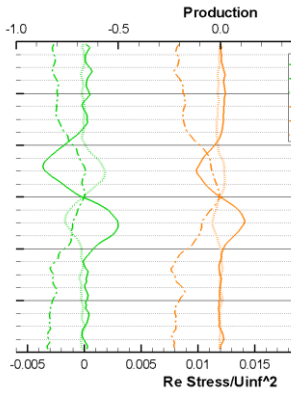
Plane C, x/c = 0.8	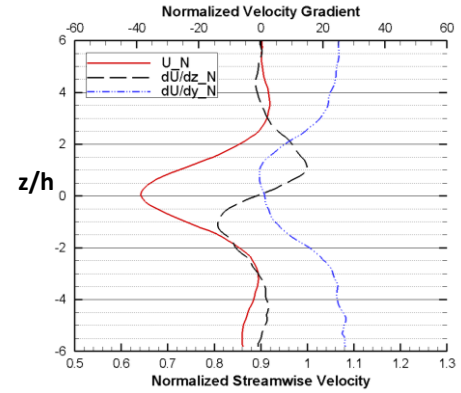	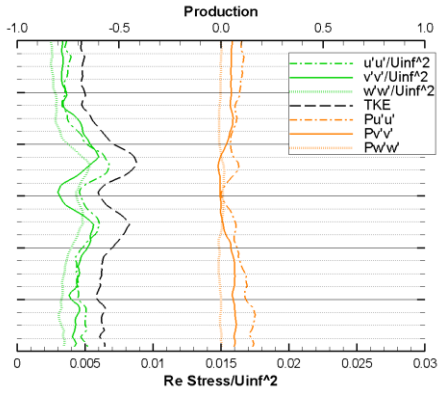	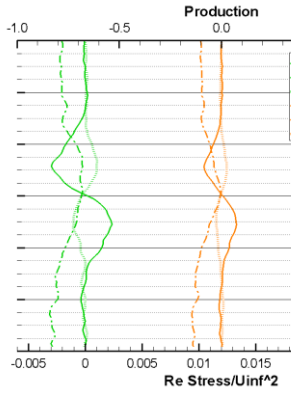

	Through the vortex centres		
Plane A, x/c = 0.6	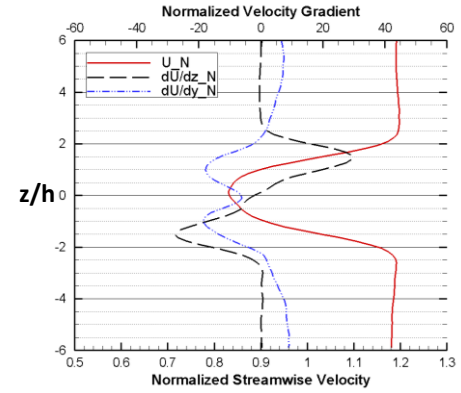	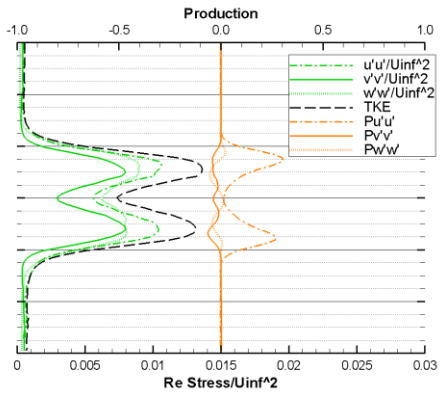	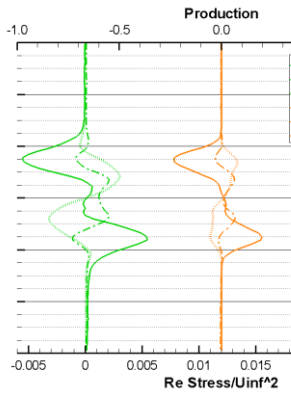
Plane B, x/c = 0.7	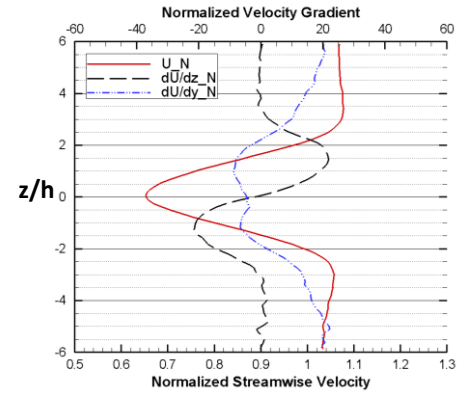	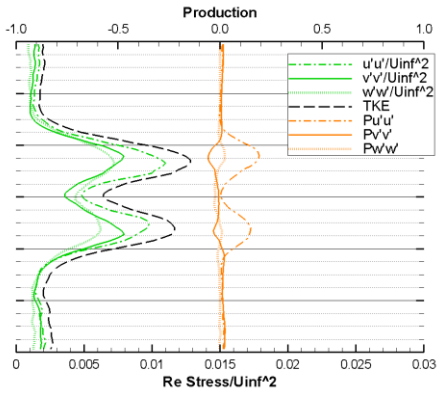	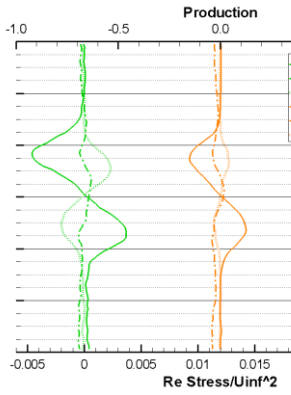
Plane C, x/c = 0.8	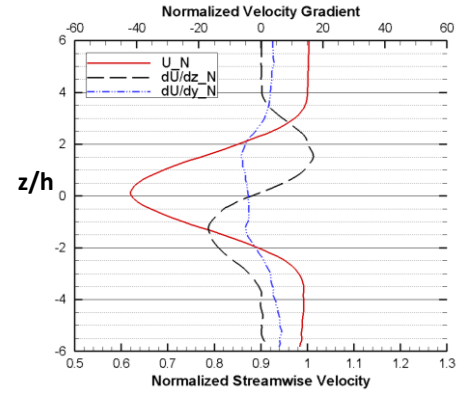	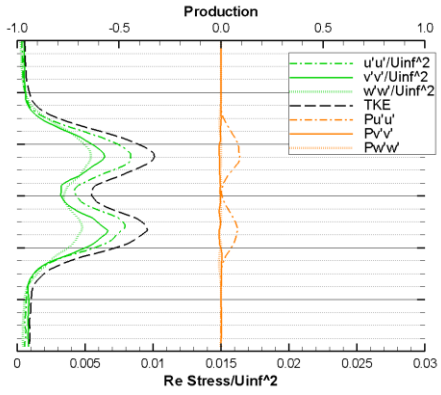	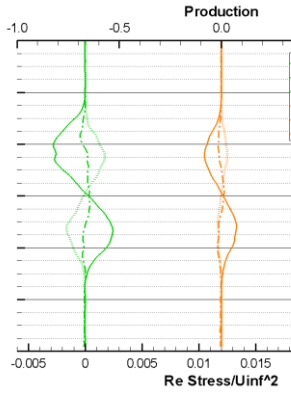

	Top part of the vortex pair		
Plane A, x/c = 0.6	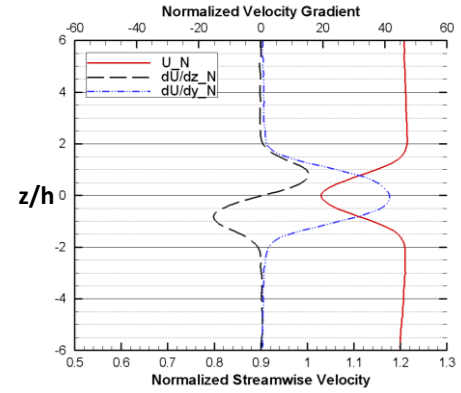	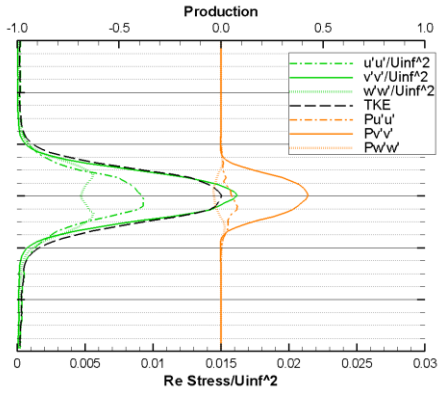	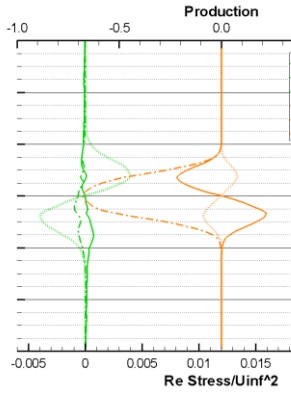
Plane B, x/c = 0.7	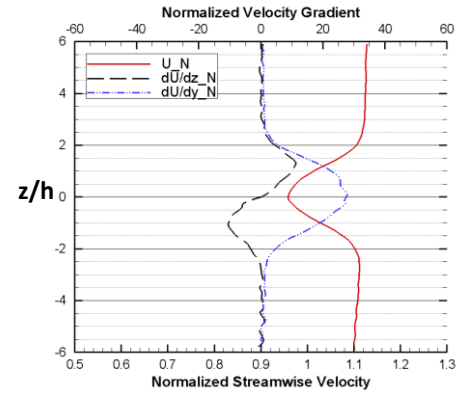	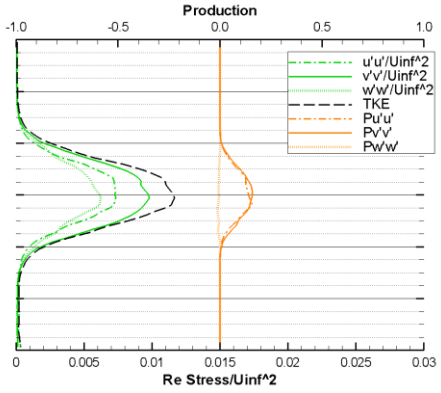	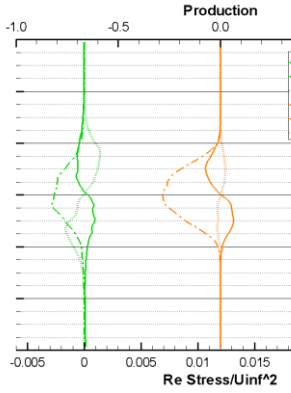
Plane C, x/c = 0.8	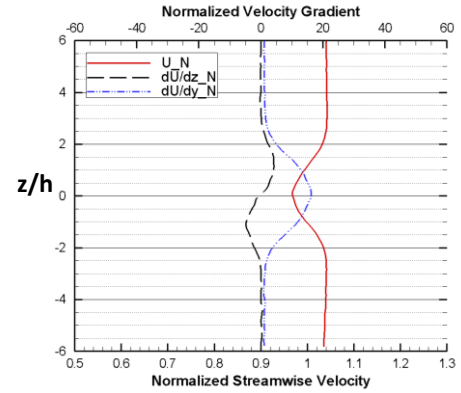	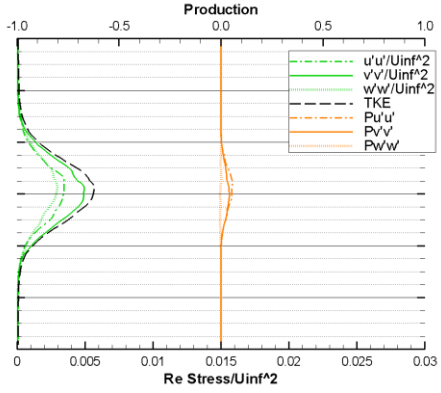	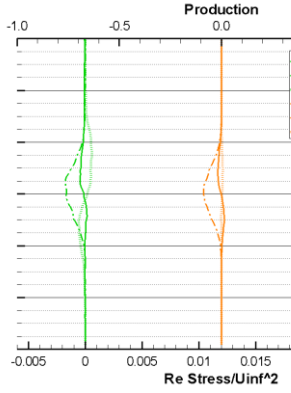

4 Conclusions

The effect of passive vortex generators on the performance of a wind turbine airfoil exhibiting 3D separation of the Stall Cell type has been investigated experimentally. Counter-rotating triangular vanes with common flow up have been used. The reported data include pressure recordings at mid-span (on the wing surface and the wake) and Stereo PIV measurements at three chordwise stations positioned at 27.2, 37.2 and 47.2 VG heights downstream of the VG TE. Based on these data a detailed analysis of the flow is carried out revealing new features of the way VGs affect the onset of SCs on airfoils and of VG induced flow. The main findings are summarized below.

It is found that SC formation can be delayed by 5°, resulting in significantly higher lift up to $\alpha = 15°$. At lower incidences ($\alpha < 6°$) a drag penalty of $\Delta Cd = 0.002$, inherent in passive VGs, was also measured. At 16° the flow bifurcated between two distinct states: a dominant High Lift state, in which the flow was mostly attached and a less frequent Low Lift state, when a large stall cell was formed. This bifurcating behaviour is associated with the state of the VG vortices, which can lead to SC re-establishment. The switching from one state to the other is intermittent and the less frequent Low Lift state lasted for a limited amount of time (less than 3sec for measurements of up to 180sec).

It is noted that this bifurcating behaviour is different from the usually mentioned unstable nature of SCs with no flow control. In the latter case the SCs move in the spanwise direction or form and disappear in a seemingly random manner, however, there is always at least a single SC on the wing at some spanwise location. What was observed in the experiments presented here was a bifurcation between a case with and a case without a SC.

The interpretation of the flow structure past the VGs as revealed by the Stereo PIV data is in agreement with previous studies conducted on flat plates with or without pressure gradient. From the presented results it is clear that for the space range considered, the averaged data show that the VG vortices grow in size and move away from each other and away from the wing surface during their downstream evolution. The streamwise velocity profile has a double peak due to high velocity flow being entrained by the VG vortices close to the wing surface.

A detailed analysis of the Re Stress quantities and mean flow gradients is presented for the first time for this type of flow. Mean flow velocity gradients are well correlated to regions of intense turbulent transport, as indicated by high shear Re stresses and supported by the examination of the corresponding production terms. Regions of high normal Re stresses are well correlated to regions of high flow shear, while excessively strong $\overline{v'v'}$ indicates spanwise wandering of the vortices.

The combined conclusion, from vortex evolution, vorticity contours and the distribution of turbulent quantities, is that up to the second measurement plane (37.2h downstream of the VG TE), turbulent transport between the VG vortices and the underlying flow is strong while from the second plane to the third (47.2h downstream of the VG TE) diffusion becomes the main mechanism that governs the flow.

Acknowledgements

The authors would like to thank Onassis Foundation for their support through the G ZF 032 / 2009-2010 scholarship grant.

Appendix

Wind tunnel and wing model

The NTUA wind tunnel is of the closed single-return type and the free-stream turbulence level in the 3.75 m long octagonal test section is 0.2%. The wing model had a chord of 0.6m and the solid blockage of the model reached a maximum of 9.2% at the highest angle of attack $\alpha = 16^{o}$. Tuft flow visualization experiments reported in [45] showed that there was no flow "spillage" over the fences. The fences dimensions are given in Figure 24.

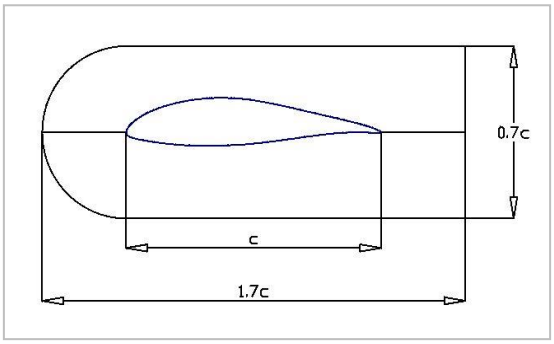

Figure 24: Airfoil profile and fences.

The model surface was painted with Rhodamine 6G, which shifts the wavelength of the impeding laser light through absorption and re-emission [61]. By applying suitable band-pass filters on the camera lenses it is possible to prevent the reflections from reaching the CCD sensors. Thus measurements closer to the surface can be performed. The technique was also used in [41]. Rhodamine 6G is a fluorescent substance and therefore a non-fluorescent pigment (TiO_2) had to be used for oil flow visualization tests.

The ZZ tape was oversized for tripping requirements, as its main use was to act as a large enough localized disturbance. Flow visualization results confirm that transition was triggered locally at the ZZ tape location, at the centre of the wing span, while free transition occurred at the sides of the ZZ tape.

The VGs were constructed by a 0.2mm thick aluminium strip that was located on wing suction surface. This is a common technique [62-64] used to ensure that the VGs will have adequate rigidity and impose minimum distortion to the boundary layer.

Pressure measurement instrumentation

62 pressure taps were distributed along the wing chord at the centre of the wing span. They extended from the leading edge up to 88.8% of the chord. All wing pressure channels were fed through a pressure scanner (model FCS421, Furness Controls Ltd) to a Furness Manometer (FCO16) and then through a 16 bit A/D card (National Instruments - USB6251) to the lab computer.

The wake rake was 39.1cm wide and consisted of 45 total pressure tubes and two static pressure tubes, located on a plane parallel, but offset with respect to the rake plane. The rake was positioned 0.82c downstream of the wing TE and could move both in the spanwise

direction and in the direction normal to the wing span. All rake tubes were connected to a Scanivalve sensor (Model J) and then to the A/D card.

Force coefficients

The lift coefficient was computed from the pressure distribution around the airfoil. Due to tap positioning, the Cl values reported in the present study refer to the 88.8% part of the profile. An analysis based on the numerical data reported in [12] showed that the experimentally measured Cl value is lower than the full profile Cl by 0.02 for angles $-5° \leq \alpha \leq 9°$ and by 0.04 for angles $10° \leq \alpha \leq 16°$.

For attached flow conditions the drag coefficient was computed from the wake pressure distribution according to [65]. For the case with VGs, drag varied significantly even under attached flow conditions due to the presence of the streamwise vortices shed by the actuators, as expected [66]. The drag was, hence, measured at four positions downstream of a VG pair and then averaged. The four measurement positions were equidistant and covered half the distance between two VG pairs. Position 0 was between the two VGs of the central VG pair and Position 3 was between the two consecutive VG pairs, see Figure 24, right. For separated flow conditions ($\alpha > 6°$ and $\alpha > 11°$ for the uncontrolled and the controlled case, respectively), drag was evaluated from the pressure measurements on the wing.

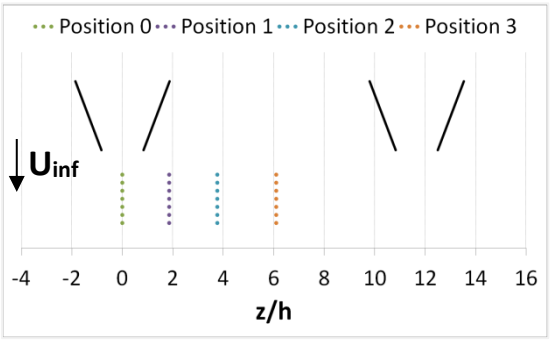

Figure 25: Drag measurement positions for the case with the VGs

Stereo PIV measurement equipment

Stereo PIV measurements were performed using a 200mJ TSI Nd:YAG PIV laser with dual cavities. The light sheet thickness at the measurement plane was 1.8mm thick. The flow was seeded with oil droplets of 1μm mean diameter created by a commercial generator (TSI model 9307). Two 12-bit TSI Powerview Plus™ 4MP Cameras with Sigma 150mm f/2.8 lenses were used to obtain the data.

Pulse separation time

In order to reduce errors associated with flow acceleration and curvature effects, a small pulse separation time should be used [54]. Furthermore, when the measurement plane is normal to the main velocity component, as in the present case, a small pulse delay is required, in order to reduce the number of particles that go out of the measurement window. However, reducing the pulse delay reduces the measurement dynamic range and increases the relevant measurement error, so a compromise is necessary. In the present case a pulse separation time of 12 μsec was used as higher values would increase the measurement noise and make peak detection harder. For all planes the number of spurious

vectors was always below 2% and the particle displacement was in all cases less than 1/4 of the 16 × 16px final interrogation areas.

Given the number of parameters involved, estimating the uncertainty in a PIV system is not trivial [67]. Under optimal conditions the minimum displacement that can be accurately estimated is 0.1px [68, 69]. The corresponding minimum resolvable velocity for a pulse separation time of 12 μsec was U_{res} = 0.4m/s. Any estimated velocity lower than U_{res} is not reliable.

Stereo PIV calibration

A dual plane target was used, allowing the calibration coefficients computation without traversing the target in the out-of-plane direction. The calibration polynomial in the free stream direction was first order [54]. The side of the target was fitted with a mirror aligned with the centreline between the two planes of one side of the target. The optical path of the reflected sheet was made co-planar with the incident sheet to ensure the best possible alignment of the laser sheet with the calibration target.

Image Processing

The image processing was done using the Insight 4G (TSI) software. In pre-processing a background reflection image was subtracted from the measurement images to remove unwanted reflections. In processing, the overlap between interrogation areas was set to 50% and a Gaussian peak estimator was used. The signal-to-noise ratio was set to 1.5 and spurious vectors were replaced using a 3x3 local mean. Peak locking was examined by checking the displacement histograms from the measured data. No peak locking was observed in the results.

References

[1] Chang P.K. 1976 *Control of flow separation: Energy conservation, operational efficiency, and safety* Hemisphere Publishing Corp Washington D. C.

[2] Gad-el-Hak M. and Bushnell D.M. 1991 Separation control: Review *Journal of Fluids Engineering* **113** 1.

[3] Seshagiri A., Cooper E. and Traub L.W. 2009 Effects of vortex generators on an airfoil at low reynolds numbers *Journal of Aircraft* **46** 1 116-122.

[4] Ashill P.R., Fulker J.L. and Hackett K.C. 2001 Research at dera on sub-boundary layer vortexgenerator s (sbvgs) *AIAA Paper* 887.

[5] Langan K.J. and Samuels J.J. 1995 Experimental investigations of maneuver performance enhancements on an advanced fighter/attack aircraft *AIAA Paper* 95-442.

[6] Aider J.-L., Beaudoin J.-F. and Wesfreid J.E. 2009 Drag and lift reduction of a 3d bluff-body using active vortex generators *Experiments in Fluids* **48** 5 771-789.

[7] Øye S. 1995 The effect of vortex generators on the performance of the elkraft 1000 kw turbine in: 9th IEA Symposium on Aerodynamics of Wind Turbines.

[8] Holmes A.E., Hickey P.K., Murphy W.R. and Hilton D.A. 1987 The application of sub-boundary layer vortex generators to reduce canopy "mach rumble" interior noise on the gulfstream iii *AIAA Paper* 87-0084.

[9] Wendt B., Reichert B.A. and Foster J.D. 1995 The decay of longitudinal vortices shed from airfoil vortex generators.

[10] Gregory N., Quincey V.G., O'Reilly C.L. and Hall D.J. 1971 Progress report on observations of three-dimensional flow patterns obtained during stall development on aerofoils, and on the problem of measuring two-dimensional characteristics. in: C.P. 1146 Aeronautical Research Council.

[11] Manolesos M. and Voutsinas S.G. 2014 Study of a stall cell using stereo particle image velocimetry *Physics of Fluids* **26** 4 045101.

[12] Manolesos M., Papadakis G. and Voutsinas S.G. 2013 Experimental and computational analysis of stall cells on rectangular wings *Wind Energy* **17** 6.

[13] Broeren A.P. and Bragg M.B. 2001 Spanwise variation in the unsteady stalling flowfields of two-dimensional airfoil models *AIAA Journal* **39** 9 1641-1651.

[14] Fuglsang P. and Bove S. 2008 Wind tunnel testing of airfoils involves more than just wall corrections. in: Proceedings of EWEA European Wind Energy Conference.

[15] Velte C.M. and Hansen M.O. 2013 Investigation of flow behind vortex generators by stereo particle image velocimetry on a thick airfoil near stall *Wind Energy* **16** 5 775-785.

[16] van Bussel G. 2012 Wakes, blades and airfoils an entangled trilogy in: Proceedings of EWEA European Wind Energy Conference Oldenburg.

[17] Sørensen N.N. and Schreck S. 2012 Computation of the national renewable energy laboratory phase-vi rotor in pitch motion during standstill *Wind Energy* **15** 3 425-442.

[18] Boorsma K., Schepers J., Gomez-Iradi S., Madsen H.A., Sørensen N., Shen W.Z., Schulz C. and Schreck S. 2014 Mexnext-ii: The latest result on experimental wind turbine aerodynamics in: EWEA Conference 2014 Barcelona.

[19] LöGdberg O., Fransson J.H.M. and Alfredsson P.H. 2009 Streamwise evolution of longitudinal vortices in a turbulent boundary layer *Journal of Fluid Mechanics* **623**.

[20] Liu J., Piomelli U. and Spalart P.R. 1996 Interaction between a spatially growing turbulent boundary layer and embedded streamwise vortices *Journal of Fluid Mechanics* **326** -1.

[21] Angele K.P. and Muhammad-Klingmann B. 2005 The effect of streamwise vortices on the turbulence structure of a separating boundary layer *European Journal of Mechanics - B/Fluids* **24** 5 539-554.

[22] Manolesos M., Papadakis G. and Voutsinas S.G. 2014 Assessment of the cfd capabilities to predict aerodynamic flows in presence of vg arrays *Journal of Physics: Conference Series* **524** 1 012029.
[23] Rao D.M. and Kariya T.T. 1988 Boundary-layer submerged vortex generators for separation control - an exploratory study in: 1st National Fluid Dynamics Congress AIAA pp. 839-846.
[24] Pauley W.R. and Eaton J.K. 1988 Experimental study of the development of longitudinal vortex pairs embedded in a turbulent boundary layer *AIAA Journal* **26** 7 816-823.
[25] Lin J.C. 1999 Control of turbulent boundary-layer separation using micro-vortex generators *AIAA Paper* 99-993404.
[26] McCurdy W.J. 1948 Investigation of boundary layer control of an naca 16-325 airfoil by means of vortex generators *United Aircraft Corp., Research Department, Rept. M-15038-3*.
[27] Taylor H.D. 1950 Summary report on vortex generators in: Technical Report No. R-05280-9 United Aircraft Corporation. Research Dept.
[28] Schubauer G.B. and Spangenberg W.G. 1959 Forced mixing in boundary layers *Journal of Fluid Mechanics* **8** 01.
[29] Pearcey H.H. 1961 Shock induced separation and its prevention by design and boundary layer control in: G.V. Lachmann (Ed.) Boundary layer and flow control Pergamon Press pp. 1166-1344.
[30] Lin J.C. 2002 Review of research on low-profile vortex generators to control boundary-layer separation *Progress in Aerospace Sciences* **38** 4-5 389-420.
[31] Wendt B. 2004 Parametric study of vortices shed from airfoil vortex generators *AIAA Journal* **42** 11 2185-2195.
[32] Godard G. and Stanislas M. 2006 Control of a decelerating boundary layer. Part 1: Optimization of passive vortex generators *Aerospace Science and Technology* **10** 3 181-191.
[33] Mehta R.D. and Bradshaw P. 1988 Longitudinal vortices imbedded in turbulent boundary layers part 2. Vortex pair with 'common flow' upwards *Journal of Fluid Mechanics* **188** -1.
[34] Shabaka I., Mehta R. and Bradshaw P. 1985 Longitudinal vortices imbedded in turbulent boundary layers. Part 1. Single vortex *Journal of Fluid Mechanics* **155** 37-57.
[35] Angele K.P. and Grewe F. 2007 Instantaneous behavior of streamwise vortices for turbulent boundary layer separation control *Journal of Fluids Engineering* **129** 2.
[36] Yao C.S., Lin J.C. and Brian A.G. 2002 Flow-field measurement of device-induced embedded streamwise vortex on a flat plate *AIAA Paper* 3162.
[37] Westphal R.V. and Mehta R.D. 1989 Interaction of an oscillating vortex with a turbulent boundary layer *Experiments in Fluids* **7** 6 405-411.
[38] Wokoeck R., Krimmelbein N., Ortmanns J., Ciobaca V., Radespiel R. and Krumbein A. 2006 Rans simulation and experiments on the stall behaviour of an airfoil with laminar separation bubbles in: 44th AIAA aerospace sciences meeting and exhibit, Reno, AIAA-2006-244.
[39] Yon S.A. and Katz J. 1998 Study of the unsteady flow features on a stalled wing *AIAA Journal* **36** 3 305-312.
[40] Winkelmann A.E. and Barlow J.B. 1980 Flowfield model for a rectangular planform wing beyond stall *AIAA Journal* **18** 08 1006-1008.
[41] Velte C.M. and Hansen M.O.L. 2012 Investigation of flow behind vortex generators by stereo particle image velocimetry on a thick airfoil near stall *Wind Energy*.
[42] Schewe G. 2001 Reynolds-number effects in flow around more-or-less bluff bodies *Journal of Wind Engineering and Industrial Aerodynamics* **89** 1267-1289.
[43] Zarutskaya T. and Arieli R. 2005 On vortical flow structures at wing stall and beyond in: 35th AIAA Fluid Dynamics Conference and Exhibit pp. 1-10.

[44] Gregory N. and O'Reilly C.L. 1970 Low-speed aerodynamic characteristics of naca 0012 aerofoil section, including the effects of upper-surface roughness simulating hoar frost in: Research & Memoranda - 3726 Aeronautical Research Council.
[45] Manolesos M. and Voutsinas S.G. 2013 Geometrical characterization of stall cells on rectangular wings *Wind Energy* **17** 9 1301-1314.
[46] Moss G.F. and Murdin P.M. 1971 *Two-dimensional low-speed tunnel tests on the naca 0012 section including measurements made during pitching oscillations at the stall* 1st ed. H.M. Stationery Office London.
[47] Storms B.L. and Jang C.S. 1994 Lift enhancement of an airfoil using a gurney flap and vortex generators *Journal of Aircraft* **31** 3 542-547.
[48] Mourikis D., Riziotis V. and Voutsinas S. 2004 Aerodynamic design using genetic algorithms and application to rotor blades in: Proceedings of the International Conference on Computational and Experimental Engineering and Sciences, ICCES pp. 26-29.
[49] Bian S., Ceccio S.L. and Driscoll J.F. 2009 A dual-camera cinematographic piv measurement system at kilohertz frame rate for high-speed, unsteady flows *Experiments in Fluids* **48** 3 487-495.
[50] Bremner D.M., Hutcheson F.V. and Stead D.J. 2005 Methodology for the elimination of reflection and system vibration effects in particle image velocimetry data processing. in: NASA/TM-2005-213257; L-19028
[51] Krothapalli A., Venkatakrishnan L., Lourenco L., Greska B. and Elavarasan R. 2003 Turbulence and noise suppression of a high-speed jet by water injection *Journal of Fluid Mechanics* **491** 131-159.
[52] Kang D.H., Longo J., Marquardt M. and Stern F. 2008 Solid/free-surface juncture boundary layer and wake with waves in: 27th Symposium on Naval Hydrodynamics.
[53] Manolesos M. 2013 *Experimental and computational investigation of three-dimensional separation and separation control using passive vortex generators* NTUA PhD Thesis, Athens http://www.aerolab.mech.ntua.gr/Manolesos%20PhD.pdf.
[54] Ramasamy M. and Leishman J.G. 2006 Benchmarking piv with ldv for rotor wake vortex flows in: 24 th AIAA Applied Aerodynamics Conference.
[55] Ramasamy M., Paetzel R. and Bhagwat M.J. 2011 Aperiodicity correction for rotor tip vortex measurements in: Proceedings of the American Helicopter Society 67th annual national forum.
[56] Martin P.B., Leishman J., Pugliese G.J. and Anderson S.L. 2000 Stereoscopic piv measurements in the wake of a hovering rotor in: AHS International, Annual Forum, 56 th, Virginia Beach, VA pp. 402-420.
[57] Raffel M., Kompenhans J. and Willert C.E. 1998 *Particle image velocimetry: A practical guide* Springer Berlin.
[58] Kolář V. 2007 Vortex identification: New requirements and limitations *International Journal of Heat and Fluid Flow* **28** 4 638-652.
[59] Stillfried F.V., Wallin S. and Johansson A.V. 2011 Evaluation of a vortex generator model in adverse pressure gradient boundary layers *AIAA Journal* **49** 5 982-993.
[60] Pope S.B. 2000 *Turbulent flows* Cambridge University Press Cambridge ; New York.
[61] Kubin R.F. and Fletcher A.N. 1982 Fluorescence quantum yields of some rhodamine dyes *Journal of Luminescence* **27** 4 455-462.
[62] Fuglsang P., Antoniou I., Dahl K.S. and Aagaard Madsen H. 1998 Wind tunnel tests of the ffa-w3-241, ffa-w3-301 and naca 63-430 airfoils. in: Risø-R 1041.
[63] Bak C., Fuglsang P., Johansen J. and Antoniou I. 2000 Wind tunnel tests of the naca 63-415 and a modified naca 63-415 airfoil in: Risø-R-1193.
[64] Fuglsang P., Bak C., Gaunaa M. and Antoniou I. 2003 Wind tunnel tests of risø-b1-18 and risø-b1-24. in: Risø-R-1375.

[65] Barlow J.B., Rae W.H. and Pope A. 1999 *Low-speed wind tunnel testing* John Wiley & Sons New York.
[66] Timmer W.A. and Van Rooij R.P.J.O.M. 2003 Summary of the delft university wind turbine dedicated airfoils *Journal of Solar Energy Engineering* **125** 4 488-496.
[67] Willert C. 1997 Stereoscopic digital particle image velocimetry for application in wind tunnel flows *Measurement Science and Technology* **8** 12 1465-1479.
[68] Westerweel J. 2000 Theoretical analysis of the measurement precision in particle image velocimetry *Experiments in Fluids* **29** 1 S003-S012.
[69] Foucaut J.M., Miliat B., Perenne N. and Stanislas M. 2004 Characterization of different piv algorithms using the europiv synthetic image generator and real images from a turbulent boundary layer in: Particle image velocimetry: Recent improvements Springer pp. 163-185.